Geophysical Prospecting

EAGE EUROPEAN ASSOCIATION OF GEOSCIENTISTS & ENGINEERS

Geophysical Prospecting, 2019, **67**, 1404–1430 doi: 10.1111/1365-2478.12782

Bulk moduli and seismic attenuation in partially saturated rocks: hysteresis of liquid bridges effect

Alexander Y. Rozhko*

Department of Energy Resources, University of Stavanger, Stavanger, Norway

Received June 2018, revision accepted March 2019

ABSTRACT

A key task of exploration geophysics is to find relationships between seismic attributes (velocities and attenuation) and fluid properties (saturation and pore pressure). Experimental data suggest that at least three different factors affect these relationships, which are not well explained by classical Gassmann, Biot, squirt-flow, mesoscopic-flow and gas dissolution/exsolution models. Some of these additional factors include (i) effect of wettability and surface tension between immiscible fluids, (ii) saturation history effects (drainage versus imbibition) and (iii) effects of wave amplitude and effective stress. We apply a new rock physics model to explain the role of all these additional factors on seismic properties of a partially saturated rock. The model is based on a well-known effect in surface chemistry: hysteresis of liquid bridges. This effect is taking place in cracks, which are partially saturated with two immiscible fluids. Using our model, we investigated (i) physical factors affecting empirical Brie correlation for effective bulk modulus of fluid, (ii) the role of liquids on seismic attenuation in the low frequency (static) limit, (iii) water-weakening effects and (iv) saturation history effects. Our model is applicable in the low frequency limit (seismic frequencies) when capillary forces dominate over viscous forces during wave-induced two-phase fluid flow. The model is relevant for the seismic characterization of immiscible fluids with high contrast in compressibilities, that is, for shallow gas exploration and CO_2 monitoring.

Key words: Rock physics, surface phenomena, seismic rock properties, partial saturation.

1 INTRODUCTION

Key challenges of shallow gas exploration and CO_2 monitoring are finding relationships between seismic attributes (velocities and attenuation) and fluid properties (saturation and pore pressure). Several factors affect seismic velocities, which are not well explained by Gassmann, Biot, squirt-flow, mesoscopic-flow and gas dissolution/exsolution models. The effect of surface phenomena on elastic wave velocity in porous media has been observed 70 years ago, after Wyllie, Gregory and Gardner (1958) who observed the effect of wettability on seismic wave velocity. More recent work of Wang, Schmitt and Wang (2015) suggests that the discrepancy between the experimental data and Biot–Gassmann models is related to the slip at the solid–fluid interface, where the slip condition depends on the wettability of the rock (Lauga, Brenner and Stone 2007). Wang *et al.* (2015) argued that, due to the slippage at the solid–fluid interface, the stiffness of the rock will be lower than predicted by Biot–Gassmann models, which assume Stoke's no-slip boundary conditions between fluid and solid. Knight *et al.* (2010) argued that the change of seismic velocities observed during drainage and imbibition is related to the change of the interfacial area between immiscible fluids. Furthermore, Knight *et al.* (2010) argued that the bridges of interface menisci restrict the relative motion

*E-mail: alexander.y.rozhko@uis.no

of immiscible fluids during wave-induced fluid flow, which increases the apparent stiffness of the rock. This implies that two competing processes are taking place on the interfaces between gas, liquid and solid:

1. The presence of interface menisci and the contact-line pinning effects restrict the relative motion of the fluids during wave-induced two-phase fluid flow, causing increase in the effective stiffness of a partially saturated rock;

2. Wettability-dependent Stoke's no-slip boundary condition may not always apply in submicron pores and at the contact line location, causing the fluid molecule to slip and roll over the surface of solid. This reduces the effective stiffness of a partially saturated rock and causes the attenuation of wave energy.

Murphy (1984) and Murphy, Winkler and Kleinberg (1986) suggested the model, explaining the frame modulus reduction in sedimentary rocks due to the effect of adsorption on a grain contact. They demonstrated that the water-weakening effect is taking place even in unconsolidated sandstones, which excludes other water-weakening mechanisms, such as swelling of clay cement, osmotic suction and dissolution and precipitation of calcite. The review of different water-weakening mechanisms of dynamic rock moduli can be found in Li *et al.* (2017).

Previous research suggested that the impact of partial saturation on the bulk modulus can be attributed to an effective fluid modulus of a single-phase fluid (e.g. Mavko, Mukerji and Dvorkin 2009; Papageorgiou, Amalokwu and Chapman 2016). Mavko and Mukerji (1998) proposed upper and lower bounds (Voigt and Reuss bounds) on low-frequency seismic velocity in a partially saturated rock. Their model considers different averaging methods (isostrain versus isostress) for the effective bulk moduli of the fluid and do not consider any solid–fluid and fluid–fluid interactions, which can potentially change these bounds and explain the diversity of the experimental results.

Brie *et al.* (1995) suggested an empirical correlation between effective fluid bulk modulus and gas saturation. Their model is consistent with the upper and lower bounds of Mavko and Mukerji (1998) and depends on the empirical parameter. Papageorgiou *et al.* (2016) demonstrated that this empirical parameter is related to pore-scale capillary effects and may not be necessarily related to the patch size, as it is usually considered (Mavko and Mukerji 1998). Similar conclusions about the importance of pore-scaled capillarity were discussed by Qi *et al.* (2014a) and Qi, Müller and Rubino (2014b). Wollner and Dvorkin (2018) argued that an effective fluid bulk modulus can be approximated by a linear combination of Voigt and Reuss bounds, depending on the elastic moduli of the rock and the pore fluids. However, the dependence of an averaging method on elastic properties of solid and fluids does not follow directly from the model of Wollner and Dvorkin (2018). They argued that the relative contrast between the gas and water is larger in a soft rock than in rock with a stiffer frame.

The group around Prof. H.A. Spetzler (e.g. Moerig *et al.* 1996; Waite, Moerig and Spetzler 1997) designed an experiment on an artificial partially saturated crack to test the effect of physicochemical interactions at liquid–gas, liquid–solid and gas–solid interfaces on seismic attenuation and stiffness. Spetzler *et al.* observed that the low frequency stiffness of a partially saturated crack is larger than the stiffness predicted by local fluid-flow models. The authors argued that the observed stiffening is related to surface tension forces between immiscible fluids, which cannot be explained by Gassmann-type models (Gassmann 1951), because Gassmann explicitly excluded capillary forces in his analysis. Moreover, these authors argued that the observed seismic attenuation is related to a contact line friction during wave-induced contact line motion, an attenuation mechanism that was not considered before. The contact line friction occurs by the slippage and rolling of fluid molecules over the surface of the solid at the contact line location, that is, in 1D (Ren and E 2007). They found that chemical contamination had a significant effect on interfacial tension and contact angle hysteresis, affecting the contact line frictional force, and a minor effect on the compressibilities and viscosities of fluids. From these experiments, the authors observed that contamination significantly affects seismic attenuation and crack stiffness in the low frequency range, which cannot be explained by the change of fluid compressibilities and the fluid viscosities. Furthermore, Moerig *et al.* (1996) observed that seismic attenuation can either increase or decrease with frequency in the range from 0.001 to 5 Hz, depending on chemical treatment of the crack surface. Available classical models (Pride, Berryman and Harris 2004; Mavko *et al.* 2009; Müller, Gurevich and Lebedev 2010) would rather predict a linear increase of seismic attenuation in the low frequency limit. It must be noted here that effects of frictional dissipation between two solids in a contact on seismic wave attenuation and dispersion are well studied (see literature overview in Yarushina and Podladtchikov 2010). Those frictional dissipation mechanisms include sliding on crack surfaces and grain boundaries, that is, it occurs over a certain surface area in 2D. Viscous dissipation during wave-induced fluid flow on various length scales occurs due to interaction of fluid molecules moving

Table 1 Input parameters for case 1

Material parameters of the rock around a crack	
Young's modulus (E)	30 GPa
Poisson's ratio (ν)	0.3
Properties of immiscible fluids inside the crack	
Water (brine) bulk modulus (K_{we})	2.69 GPa
Gas bulk modulus (K_{nw})	0.131 MPa
Surface tension (γ)	0.073 Pa × m
Advancing contact angle for wetting phase (θ_a)	50°
Receding contact angle for wetting phase (θ_r)	30°
Crack properties	
Initial crack porosity (n_c)	2×10^{-4}
Major semi-axis (a)	10^{-2} m
Aspect ratio (b/a)	10^{-3}
Effective stress	
Effective stress ($\sigma + p_{we}$)	−10 MPa

with different velocities in a bulk volume of flowing fluid, that is, in 3D, while the contact line friction occurs at the contact line location, that is, in 1D. All these attenuation mechanisms convert elastic wave energy into the heat. The equivalence between lost mechanical energy (dissipation) and an increase in temperature was discovered by James Prescott Joule in 1851.

Pride *et al.* (2004) argued that the contact line of an air–water meniscus will remain pinned in porous media during stress perturbations induced by linear seismic waves, that is, waves with the stress perturbation amplitude of $\sim (10^2 \ldots 10^4)$ Pa. As a wave passes, the menisci will bulge and change shape but will not slip away. In this paper, we demonstrate that the depinning of the contact line will occur in partially saturated cracks with aspect ratio $\sim 10^{-3} \ldots 10^{-4}$. This range of the aspect ratio is typical for sandstones and other rocks (e.g. Zimmerman 1990). Thus, Pride *et al.*'s (2004) conclusion is not applicable for compliant (soft) pores, such as microcracks. Here, by cracks in granular materials, we understand compliant pores due to imperfectly bonded grain contacts, which, mathematically, can be described by elliptical cavities (e.g. Zimmerman 1990). Furthermore, as it will be demonstrated in the paper that the depinning condition of the contact line depends also on other parameters, given in Table 1, and on boundary conditions for immiscible fluids. In this paper, we considered an isolated crack that is partially saturated with a water and gas system and demonstrated that the depinning conditions are taking place during the propagation of linear seismic waves. For an oil–water system with much lower contrast in compressibility of fluids, the depinning of the contact line will not take place in isolated crack during the propagation of linear seismic waves. Much greater wave amplitudes are required to initiate the depinning in isolated crack, partially saturated with oil and water. However, the situation will be different if the crack is connected to other pores of different compliances. For non-isolated crack, partially saturated with oil and water, the contact line will slip during the propagation of linear seismic waves. Non-isolated crack is not considered in this paper; however, in Appendix A.6 we discuss how to modify equations presented in this paper, to address the non-isolated crack case.

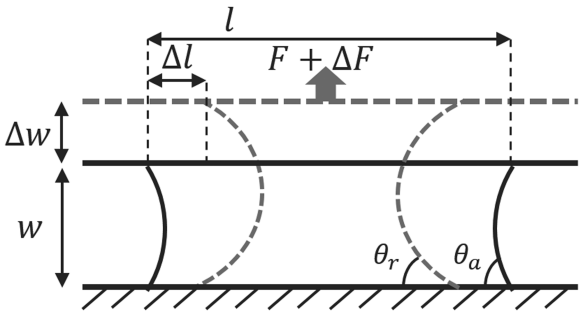

Figure 1 Deformation of the liquid bridge between two parallel plates.

In this paper, we extend the previous publication of Rozhko and Bauer (2018) by considering the hysteresis of liquid bridges' effect in the partially saturated rock. We argue that the hysteresis of liquid bridges is manifested in the form of (i) the water-weakening effect, (ii) effects of the wave amplitude, (iii) the frequency effects and (iv) the saturation history effects on seismic velocity and attenuation in the low frequency range. Furthermore, we demonstrate that this effect leads to a non-zero attenuation at zero frequency limit, where all porous diffusion-based models predict zero attenuation. We will start with introduction to published experimental data, explaining the hysteresis of liquid bridges' effect between parallel plates. In numerical examples, we investigate the influence of different physical factors affecting bulk modulus and attenuation of a partially saturated rock in the low frequency limit and addressing the "water-weakening" effects. Afterwards, we apply our model to explain the hysteresis effect of seismic properties observed during drainage and imbibition. The Appendix contains mathematical derivations of the rock physics model.

2 HYSTERESIS OF LIQUID BRIDGES BETWEEN PARALLEL PLATES (LAB DATA)

This section will introduce the hysteresis of liquid bridges, a well-known effect in surface chemistry literature (e.g. De Souza *et al.* 2008; Chen, Amirfazli and Tang 2013; Zhang 2016; Shi *et al.* 2018). Figure 1 shows a typical experimental

setup used to investigate the hysteresis of liquid bridges between parallel plates. The aperture between two plates is w, the diameter of wetted area is l and F is the force between two plates. A liquid drop is placed between two plates. The upper and the lower contact angles are θ_a and θ_r. The change of aperture within a certain time t is Δw. Aperture changes induce changes in the force ΔF and the diameter of the wetted area Δl. Experiments are typically conducted under conditions when time t is large enough so that the viscous forces can be neglected. Typically, the evaporation of the liquid drop is also neglected when the time t is not too large. Of course, the evaporation of the liquid drop may take place, but it is not necessary to consider this mechanism in the explanation of experimental data, presented below.

Figure 2 describes more details about the hysteresis of liquid bridges observed experimentally (e.g. De Souza *et al.* 2008; Chen *et al.* 2013; Zhang 2016; Shi *et al.* 2018). Figure 2(a) shows capillary force versus aperture between parallel plates; Fig. 2(b) shows contact angles versus aperture; and Fig. 2(c) shows the diameter of the wetted area versus aperture. Overall, the hysteresis of liquid bridges can be divided into four continuous stages:

1. Pinning (stretching)
2. Slipping (receding)
3. Pinning (compression)
4. Slipping (advancing)

When the contact angle is greater than the receding angle, the aperture increase will result in an increase in the force due to pinning (stage 1). This will be accompanied by a reduction in the contact angle until the receding angle is achieved when the force begins to decrease and the contact line starts to slip inward (stage 2). If the aperture starts to decrease, the contact angle begins to increase until it reaches the advancing angle (stage 3). In this stage, the pinning stage occurs again, which corresponds to the reduction of the capillary force. If the aperture keeps decreasing to the initial aperture, the contact line will slip outwards with the contact angle equal to the advancing angle (stage 4). The energy dissipated per cycle is proportional to the hysteresis area of Fig. 2(a). The contact line friction is the dominant mechanism of energy dissipation in these experiments. The intermolecular forces acting between molecules of the solid and those of the liquid, which pin the contact line to the substrate, are responsible for the contact line friction, which occurs not over the entire solid–liquid interface, but only at the three-phase line (Yaminsky 2010; Bormashenko 2013a,b). Contact line friction occurs due to the slippage and rolling of fluid molecules over the surface of the solid at the contact line location, that is, in 1D (Ren and E 2007).

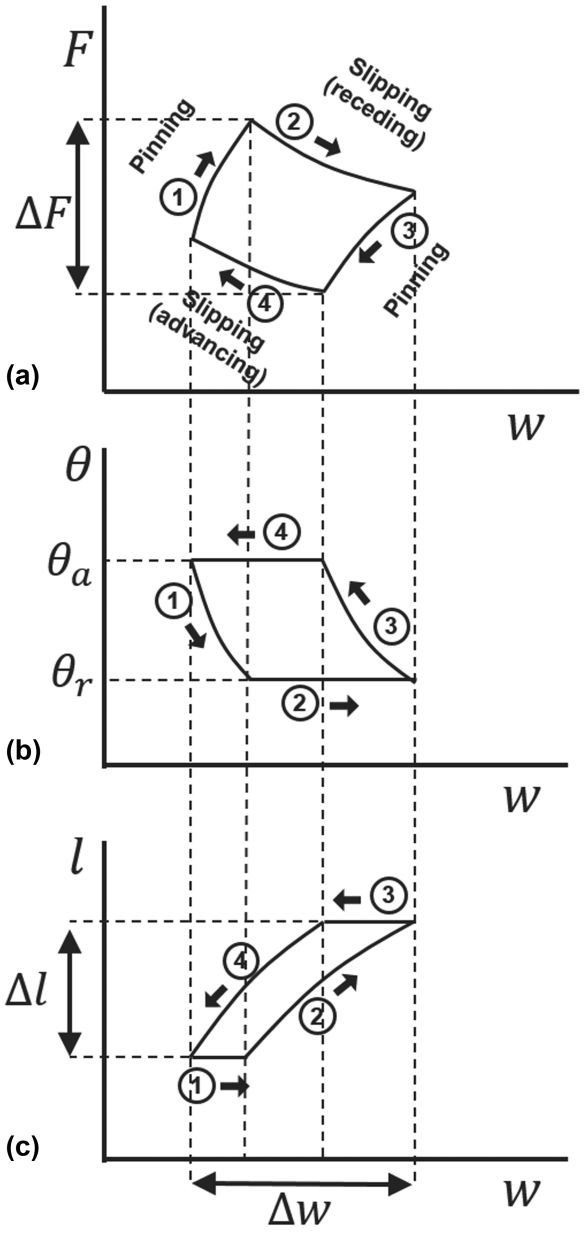

Figure 2 Schematic, four stages of liquid bridge hysteresis observed in laboratory tests (e.g. De Souza *et al.* 2008; Chen *et al.* 2013; Zhang 2016; Shi *et al.* 2018). (a) Capillary force versus aperture (between two parallel plates); (b) contact angles versus aperture; (c) diameter of the wetted area (contact line displacement) versus aperture.

Four continuous stages are possible if the amplitude of aperture deformation is sufficiently large, otherwise it will be only one periodic stage, when the contact line is pinned and the contact angle is changing within the range $\theta_r < \theta < \theta_a$.

There is no energy dissipation (by the contact line friction) when the contact line is pinned.

Viscous dissipations are also taking place in these experiments, which are proportional to the frequency of oscillations in the low frequency limit (e.g. Mavko and Nur 1979; Hudson 1988). Thus, at low frequencies, the contact line frictional dissipation may dominate over viscous dissipation. However, if the wave amplitude is small and the contact line is pinned, then the viscous dissipation will be the only dissipation mechanism in these experiments.

Contact angle hysteresis is responsible for the hysteresis of liquid bridges and contact-line friction effects (Bormashenko 2013a,b). It depends on the contact line velocity (Bonn *et al.* 2009), as shown schematically in Fig. 3(a). At zero velocity, a spectrum of static contact angles is observed (Bormashenko 2013a,b). This effect is called a static contact angle hysteresis. Figure 3(a) shows that the advancing contact angle increases with the contact line advancing velocity, while the receding contact angle decreases with the contact line receding velocity. This effect is called a dynamic contact angle hysteresis. At zero frequency limit, the contact line motion velocity is also zero, thus dynamic contact angle hysteresis can be neglected. While the static contact angle hysteresis is not zero and can be as large as tens of degrees (Ethington 1990). Thus, at low frequency, viscous dissipation is small (and thus neglected), while the contact line frictional dissipation is not small due to the static contact angle hysteresis effect.

The equilibrium configuration of the static contact line was the topic of classical work of Young, Laplace and Gauss. It is described by Young's equation, which relates the three coefficients of interfacial tension to the Young's contact angle (θ_Y) formed by the fluid–fluid interface with the solid surface (de Gennes, Brochard-Wyart and Quéré 2013). The equilibrium Young's contact angle can also be calculated from advancing and receding contact angles, as was shown theoretically by Tadmor (2004) and confirmed experimentally by Chibowski (2008).

Using the experimental setup, shown in Fig. 1, we could also investigate the effect of frequency. Figure 3(b) and 3(c) show schematically the effect of the aperture deformation velocity (i.e. frequency) increase on the hysteresis of capillary forces and contact angles, observed experimentally by Zhang (2016) and Shi *et al.* (2018). Figure 3(c) shows that with the frequency increase (when Δw is the same), the hysteresis of contact angles ($\theta_a - \theta_r$) also increase, affecting contact line pinning forces, as shown in Fig. 3(b). Figure 3(b) and 3(c) shows the manifestation of the dynamic contact angle hysteresis, which depends on the contact line velocity ($\Delta l/t$), according to Fig. 1. However, the contact line velocity depends on the aperture deformation velocity ($\Delta w/t$) and amplitude of the aperture deformation Δw. If the amplitude Δw is small, the contact line remains pinned, while the contact line is slipping if Δw is sufficiently large; thus, the frequency dependence (i.e. dependence on $1/t$) is rather non-trivial. Furthermore, with the frequency increase, viscous dissipations will also increase, which will affect, at certain stage, the experimental results, shown in Fig. 3(b) and 3(c). At this paper, we focus only on the low frequency limit, when dynamic effects of the contact angle hysteresis are neglected, and thus viscous dissipations are also neglected.

Figure 2(a) shows rather a non-trivial behaviour of the local stiffness, where the stiffness is the local slope of the force–displacement curve. According to experimental data (Fig. 2a), local stiffness can be either positive or negative. In other words, experimental data of Fig. 2(a) show that the hysteresis of the capillary force cannot be explained by Hooke's law. However, all linear theories of wave propagation are based on fundamental Hooke's law assumption. These non-trivial effects were observed experimentally between two parallel plates. We argue here that the same non-trivial effects are taking place in natural rocks. Natural rocks are very heterogeneous and anisotropic. Acoustic properties of natural rocks are affected by many factors, including pore geometry, mineral composition, saturation and distribution of pore liquids, size scale and frequency effects, rock wettability and so on. This makes it quite challenging to design good experiments for discriminating between the different possible mechanisms affecting seismic attenuation and dynamic stiffness. Many mechanisms may contribute to seismic attenuation and velocity dispersion simultaneously, including Biot's flow, scattering, squirt flow, mesoscopic flow (e.g. Pride *et al.* 2004; Mavko *et al.* 2009; Müller *et al.* 2010), plasticity and solid friction (e.g. Yarushina and Podladtchikov 2010), effects of dissolution and exsolution of gas into and from the liquid (e.g. Tisato *et al.* 2014, 2015). In laboratory experiments, we can control some of the factors influencing seismic properties, but it is very challenging to control all factors in natural rocks. At field scale, we do not have the opportunity to control the medium in the same way as in the laboratory, which means that interpretation of field results is (often – and unfortunately) prone to guesswork. This section describes the sort of "an ideal experiment": the hysteresis of liquid bridges between two parallel plates (e.g. De Souza *et al.* 2008; Chen *et al.* 2013; Zhang 2016; Shi *et al.* 2018). This effect cannot be explained by Biot's flow, scattering, squirt flow, mesoscopic flow, plasticity and solid friction,

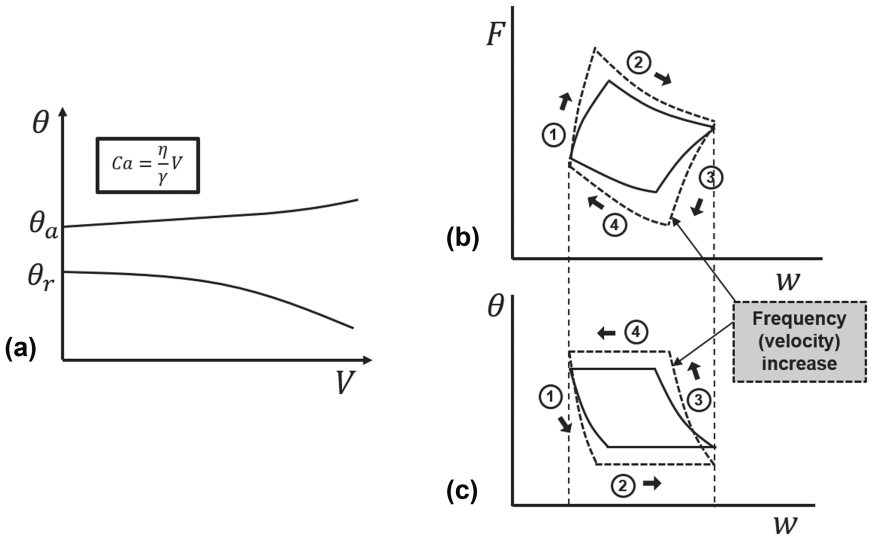

Figure 3 Frequency (velocity) effect on the hysteresis of liquid bridges. (a) Static and dynamic contact angles versus contact line velocity. At zero velocity, a spectrum of static contact angles is observed. (b) and (c) show (schematically) the frequency effect on the hysteresis of liquid bridges, based on published laboratory data (e.g. Zhang 2016; Shi *et al.* 2018). With an increase in frequency, the hysteresis of capillary force and contact angles is increased, as shown by dashed tetragons, while the amplitude of deformation remains the same.

effects of dissolution and exsolution of gas into and from the liquid, because it is related to a static contact angle hysteresis effect. A static contact angle hysteresis was not previously considered until a recent work of Rozhko and Bauer (2018). Previous authors (Miksis 1988; Moerig *et al.* 1996; Waite *et al.* 1997; Brunner and Spetzler 2001; Broadhead 2012) considered only a dynamic contact angle hysteresis in a crack that is partially saturated with a water and gas system. These authors assumed a unique value of the contact angle at zero contact line velocity. This assumption makes it impossible to explain a liquid bridge hysteresis, shown in Fig. 2, because this assumption neglects two effects: a contact line pinning and a static contact line friction. Thus, understanding of the liquid bridge hysteresis at ideal laboratory conditions will help us to understand its effect on seismic rock properties with the help of the mathematical model described in the next section.

3 HYSTERESIS OF LIQUID BRIDGES INSIDE THE CRACK (MODEL)

3.1 Rock physics model

In this section, we investigate the effect of hysteresis of liquid bridges in a partially saturated crack, shown in Fig. 4(a). The initial geometry of the crack is approximated by a deformable elliptical cavity with semi-axes a and b. In our calculations, we consider very narrow cracks, $a \gg b$. We use a 2D plane-strain approximation, widely used in geomechanics and rock physics to address 3D problems (e.g. Zimmerman 1990; Mavko *et al.* 2009; Vernik and Kachanov 2012). The wetting liquid phase occupies thin parts of the crack (tips), while the non-wetting gas phase occupies wide parts of the crack (centre). Such distribution of fluids is energetically favourable (e.g. Preuss and Tsang 1990). Previous research (e.g. Mavko and Nur 1979; Hudson 1988; Miksis 1988) considered the distribution of fluids where the liquid phase occupied the central part of the crack. This distribution is possible, but energetically not favourable and is discussed in Section 4.4. Pressures in the non-wetting (p_{nw}) and wetting (p_{we}) fluid phases are different due to interfacial tension and denoted here as capillary pressure (p_{cap}) (e.g. Barenblatt, Entov and Ryzhik 1990):

$$p_{\mathrm{cap}} = p_{\mathrm{nw}} - p_{\mathrm{we}}. \tag{1}$$

The fluid pressure acting on the crack surface is p_{nw} if $|x| \le c$ and p_{we} if $c < |x| \le a$. The coordinate $|x| = c$ defines the location of the contact line, as shown in Fig. 4(a) and 4(b). To simplify calculations, we consider the case that is independent of the crack orientation with respect to the confining stress and wave propagation directions. Therefore, we consider a uniform far-field confining stress σ, acting on the external boundary of the representative elementary volume (REV), as shown in Fig. 4(a). Our equations can still be applied to more general case, if the hydrostatic confining stress and wave-induced stress perturbations are replaced with its normal components, acting on the crack surface. Our rock physics model is based on a recently published analytical solution describing equilibrium stresses and displacements around partially saturated cracks (Rozhko 2016). This

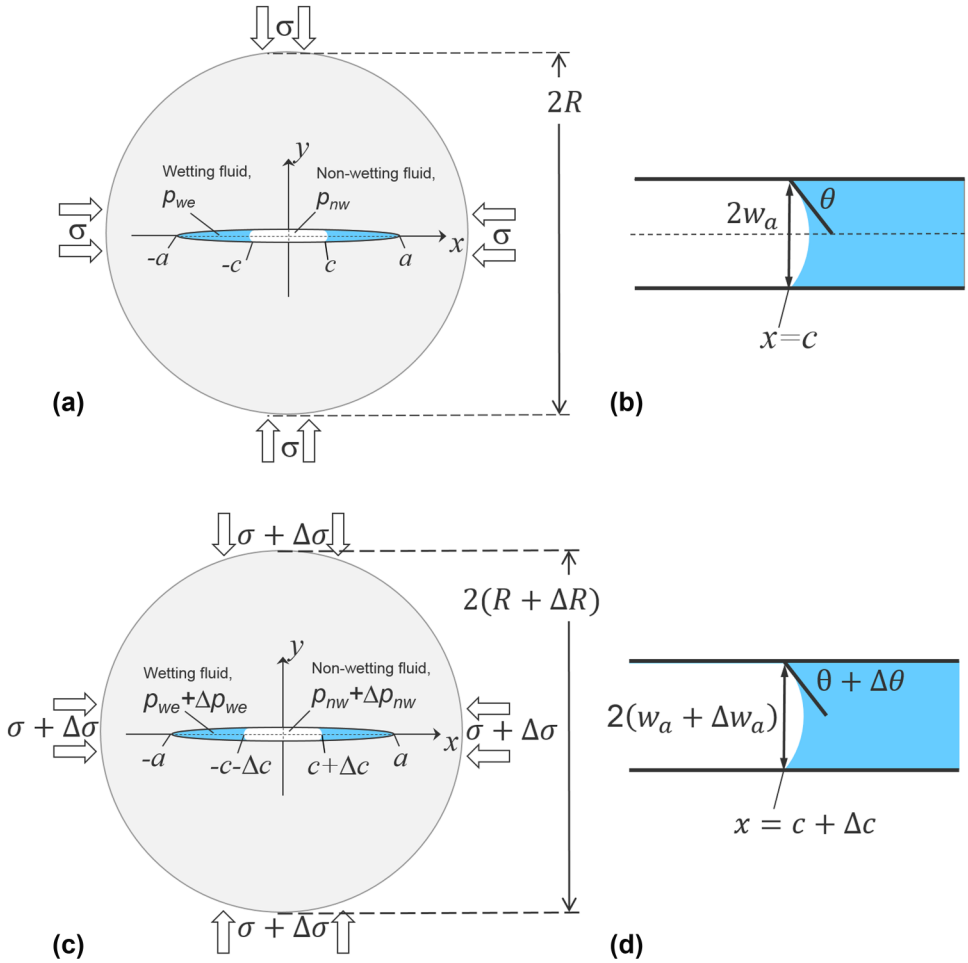

Figure 4 (a) Partially saturated crack (modified after Rozhko and Bauer 2018), plane-strain (2D) approximation. The wetting fluid phase symmetrically occupies the crack tips while the non-wetting phase is in the centre. (b) The contact angle of the wetting phase with the crack surface is θ. The coordinate $|x| = c$ defines the location of the contact line. (c and d) Perturbation of the far-field total stress ($\Delta\sigma$) along the external boundary of an REV. The change in stress induces deformations of the crack and REV (Δw_a, ΔR), as well as changes in pressures (Δp_{we}, Δp_{nw}) and volumes of the wetting and non-wetting fluid phases (ΔV_{we}, ΔV_{nw}), contact angle ($\Delta\theta$) and contact line location (Δc).

analytical solution was derived using the method of complex potentials (Muskhelishvili 1977) and conformal mapping methods (Lavrentiev and Shabbat 1973). The capillary pressure predicted by our model using the classical Young–Laplace equation is two-way coupled to crack aperture changes. Appendix A.1 provides analytical solutions predicting capillary pressure (p_{cap}), total crack volume (V_{tot}) and volume of the wetting phase (V_{we}) at the equilibrium. Those equations depend on static contact angle (θ), surface tension between liquid and gas (γ), crack length (a), contact line location (c) and initial aspect ratio (b/a), far-field confining stress (σ), pressure in the wetting phase (p_{we}), Young's modulus (E) and Poisson's ratio (v) of the rock around the crack.

Next, we consider the perturbations of the equilibrium state caused by a change in stress (as, e.g., induced by a seismic wave). The strain amplitude induced by seismic waves, which can be recorded by seismometers, is very small, typically around 10^{-8} to 10^{-6} (dimensionless units). For the rock with Young's modulus of $E \sim 10$ GPa, this strain induces stress perturbations around $\Delta\sigma \sim 10^2$ to 10^4 Pa, which correspond to the stress perturbation range induced by linear seismic waves.

Figure 4(c) shows an isotropic perturbation of the far-field total stress ($\Delta\sigma$) along the external boundary of REV. Again, for simplicity, we consider the case independent of the crack orientation; therefore, a uniform (isotropic) stress

perturbation is considered on the external boundary of REV. The size of REV (R) is much smaller than the wavelength; therefore, $\Delta\sigma$ is uniform. Perturbation of the far-field total stress ($\Delta\sigma$) induces perturbations to the following parameters: the total crack volume ΔV_{tot}, the volume of the wetting phase inside the crack ΔV_{we}, pressure in the wetting phase inside the crack Δp_{we}, capillary pressure Δp_{cap}, contact line location Δc and contact angle $\Delta\theta$. There is no liquid or gas flow in or out of the crack during the wave period, that is, undrained boundary conditions for both fluid phases are used in calculations. Thus, in our model, the masses of the wetting fluid and non-wetting fluid remain the same in the crack. In this case, changes of volumes of the wetting and non-wetting fluid phases are related to changes of pressures in those phases via the bulk moduli of the wetting (K_{we}) and non-wetting (K_{nw}) fluid phases as follows:

$$\Delta V_{\text{we}}\, K_{\text{we}} = -V_{\text{we}}\, \Delta p_{\text{we}} \tag{2}$$

and

$$\Delta V_{\text{nw}}\, K_{\text{nw}} = -V_{\text{nw}}\, \Delta p_{\text{nw}}. \tag{3}$$

The contact line slipping condition can be described by a critical stress perturbation, $\Delta\sigma_c$, required for the onset of the contact line motion. When the wave-induced stress perturbation is sufficiently small, that is, when $|\Delta\sigma| \le |\Delta\sigma_c|$, the contact line will be pinned to the crack surface, and wave-induced deformations will only cause bending of the liquid–gas interface meniscus. Otherwise, when $|\Delta\sigma| > |\Delta\sigma_c|$, the contact line will move. Here, $\Delta\sigma_c$ is calculated analytically in Appendix A.2. If $|\Delta\sigma| > |\Delta\sigma_c|$, the wave-induced deformation of REV can be split into two parts: when the contact line is pinned and when the contact line is moving. These two parts are described by a different set of equations derived in Appendix A.2. The analytic model described in Appendix A.2 is based on linearization (Taylor's expansion) of equilibrium equations of Appendix A.1 together with mass conservation equations (2) and (3) of this section. Additionally, we use iterations to solve the system of equations, since not all parameters are small during the propagation of linear seismic waves with a strain amplitude of 10^{-8} to 10^{-6} (or stress amplitudes of $\Delta\sigma \sim 10^2$ to10^4 Pa). As demonstrated below, changes of contact angles are not small ($\Delta\theta \sim \theta_a - \theta_r$) during linear seismic wave propagation. Thus, we consider the iteration parameter N_{iter}, which satisfies the condition $\frac{\theta_a - \theta_r}{N_{\text{iter}}} \ll 1$, required for Taylor's expansion (see Appendix A.4 for details).

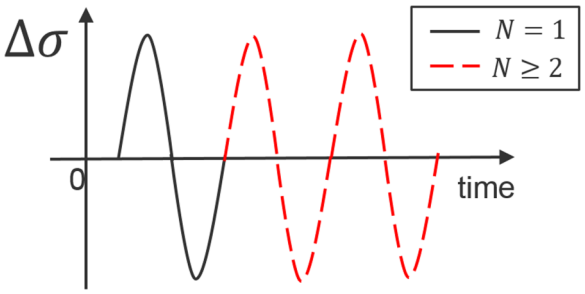

Figure 5 Periodic stress perturbation, acting on the external boundary of REV. The first cycle ($N = 1$) is shown by continuous black curve; subsequent cycles are shown by the red dashed curve.

3.2 Effect of wave amplitude on the hysteresis of liquid bridges

Next, we investigate numerically the effect of wave amplitude on the hysteresis of liquid bridges inside partially saturated crack. In calculations, we apply a periodic stress perturbation to the external boundary of REV, as shown in Fig. 5. The first ($N = 1$) cycle is shown by a continuous black curve while subsequent cycles ($N \ge 2$) are shown by the red dashed curve.

In calculations, we will investigate the effect of wave amplitude on changes of six independent parameters:

A. total crack volume ΔV_{tot};
B. contact angle $\Delta\theta$;
C. contact line location Δc;
D. capillary pressure Δp_{cap};
E. pressure in the wetting phase inside the crack Δp_{we};
F. volume of the wetting phase inside the crack ΔV_{we}.

These parameters are predicted by equations derived in Appendix A.2. These six parameters are independent, which implies that changes of other parameters (ΔS_{we}= changes of crack saturation, $2\Delta w_a$= changes of crack aperture, etc.) can be related to changes of the above six independent parameters. Thus, only independent parameters will be investigated in this section. For simplicity, some of the parameters will be displayed in dimensionless units, such as $\Delta V_{\text{tot}}/V_{\text{tot}}$, $\Delta V_{\text{we}}/V_{\text{tot}}$ and $\Delta c/b$. The following amplitudes of the applied periodic stress perturbation ($\Delta\sigma$) will be considered: 1, 5 and 50 kPa. Initial crack saturation considered in calculations below is $S_{we} = 0.75$. Other input parameters to calculations are given in Table 1. In calculation, we considered that the initial contact angle is equal to equilibrium Young's angle, calculated using Tadmor's (2004) equation (see also Rozhko and Bauer 2018), giving approximately the intermediate result

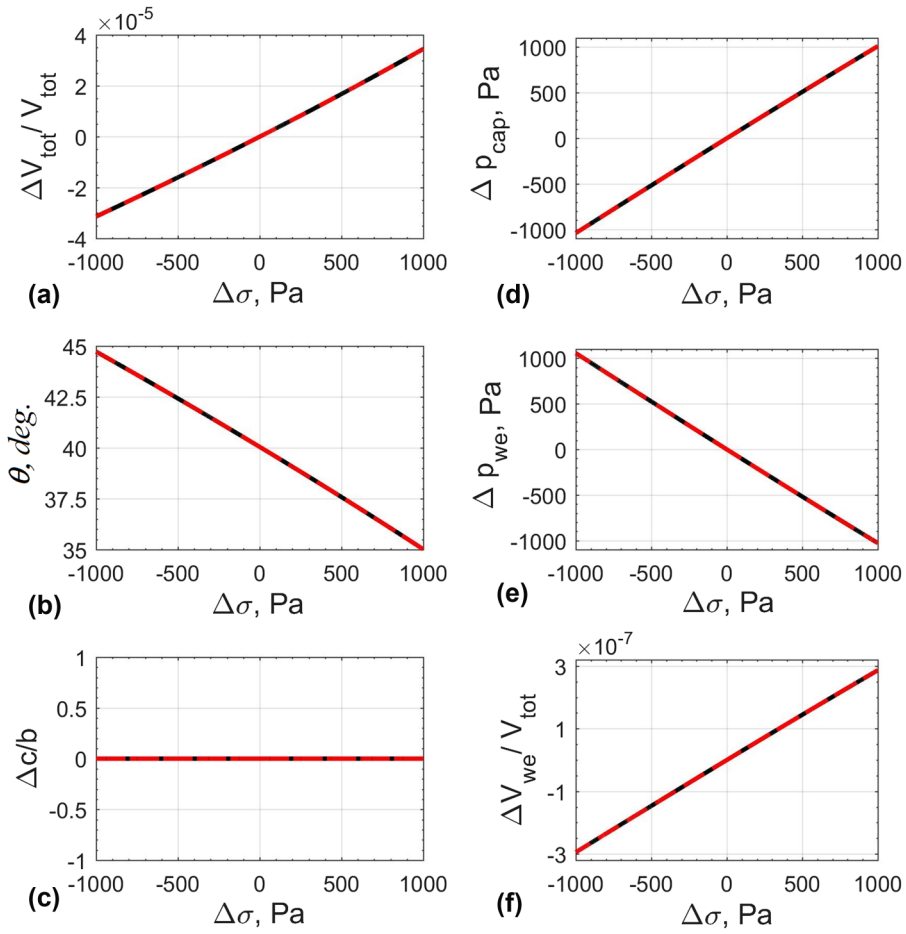

Figure 6 Effect of the hysteresis of liquid bridges on (a) changes of the crack volume (dimensionless units); (b) changes of contact angle (degrees); (c) contact line displacement (dimensionless units); (d) changes of capillary pressure (Pa); (e) changes of pressure in the wetting phase (Pa); (f) changes of the wetting phase volume inside the crack (dimensionless units). Horizontal axis shows the magnitude of transient stress (Pa). Initial (equilibrium) crack saturation is $S_{we} = 0.75$. The initial contact angle is equal to the Young's angle. Other input parameters are given in Table 1. The amplitude of the applied periodic stress perturbation ($\Delta\sigma$) is 1 kPa. Similar to Fig. 5, the first cycle ($N = 1$) is shown by a continuous black curve, while subsequent cycles are shown by a red dashed curve.

($\theta_Y \approx 40^\circ$) between the advancing ($\theta_a = 50^\circ$) and receding ($\theta_r = 30^\circ$) angles.

The case when the amplitude of applied periodic stress perturbation ($\Delta\sigma$) is 1 kPa is shown in Fig. 6(a–f). In this case, the amplitude of the applied periodic stress perturbation ($\Delta\sigma$) is too small to cause the slippage of the contact line, as shown in Fig. 6(c). Figure 6(b) shows that changes of the contact angle are in the range $\theta_r < \theta < \theta_a$. Figure 6(a) shows that the change of the crack volume is linear with no hysteresis; thus, the elastic energy is not dissipated by the contact line friction effect. Changes of the capillary pressure Δp_{cap} (in Fig. 6d) and pressure in the wetting phase Δp_{we} (in Fig. 6e) are also linear with no hysteresis effects. Amplitudes of Δp_{cap} and Δp_{we} are dependent on the choice of input parameters. In this case, amplitudes of Δp_{cap} and Δp_{we} (shown in Fig. 6d and 6e) are nearly equal to the amplitude of $\Delta\sigma$, while amplitudes could be different if input parameters are changed. Changes of volume of the wetting phase ΔV_{we} (in Fig. 6f) are much smaller than changes of the total crack volume ($\Delta V_{tot} = \Delta V_{we} + \Delta V_{nw}$), because a gas is much more compressible than water. Calculations (Fig. 6) show that when the contact line is pinned, there is no hysteresis in changes of six independent parameters.

The case when the amplitude of applied periodic stress perturbation ($\Delta\sigma$) is 5 kPa is shown in Fig. 7(a–f). In this case, the amplitude of the applied periodic stress perturbation ($\Delta\sigma$) is sufficient to cause the slippage of the contact line, as shown in Fig. 7(c). In this case, the model predicts the hysteresis of

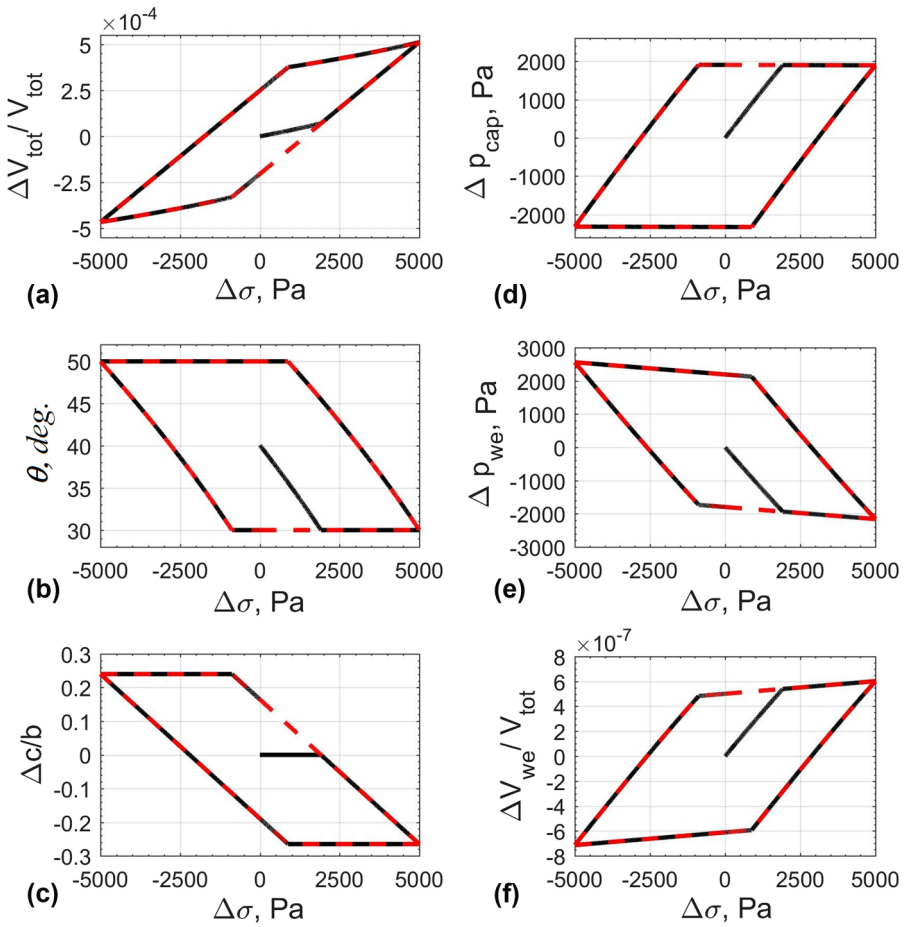

Figure 7 Effect of the hysteresis of liquid bridges on (a) changes of the crack volume (dimensionless units); (b) changes of contact angle (degrees); (c) contact line displacement (dimensionless units); (d) changes of capillary pressure (Pa); (e) changes of pressure in the wetting phase (Pa); (f) changes of the wetting phase volume inside the crack (dimensionless units). Horizontal axis shows the magnitude of transient stress (Pa). The initial (equilibrium) crack saturation is $S_{we} = 0.75$. The initial contact angle is equal to the Young's angle. Other input parameters are given in Table 1. The amplitude of applied periodic stress perturbation ($\Delta\sigma$) is 5 kPa. Similar to Fig. 5, the first cycle ($N = 1$) is shown by a continuous black curve, while subsequent cycles are shown by a red dashed curve.

all six independent parameters. The elastic wave energy is dissipated to the heat in this case, due to hysteresis effect, according to equation (9). Similar to Fig. 5, the first cycle ($N = 1$) is shown by a continuous black curve, while subsequent cycles are shown by the red dashed curve. Figure 7 shows that subsequent cycles (red dashed curves) follow the same path and will not return to the initial state. It implies that the passage of elastic waves will induce the residual changes of all six independent parameters. The residual changes of fluid pressure and porosity, caused by the passage of seismic waves, were reported in various publications (see Manga *et al.* 2012 for literature review) and predicted by our model. Similar to laboratory data (Fig. 2), there are four stages of the hysteresis of liquid bridges inside partially saturated crack, predicted in Fig. 7(a–f):

1. Pinning (stretching)
2. Slipping (receding)
3. Pinning (compression)
4. Slipping (advancing)

It is interesting to note here that the change of the applied stress by a factor 5 caused the change of crack porosity by a factor 17, as shown in Figs 6(a) and 7(a). When the contact line is pinned, the interface menisci restricts the relative motion of fluids during the wave-induced fluid flow, while when the contact line is slipping, the fluids can move and the stiffness of the partially saturated crack is much lower. It explains a highly non-linear scaling of the crack porosity (volume) perturbation with applied stress perturbation. It is possible to demonstrate that this scaling can be even more

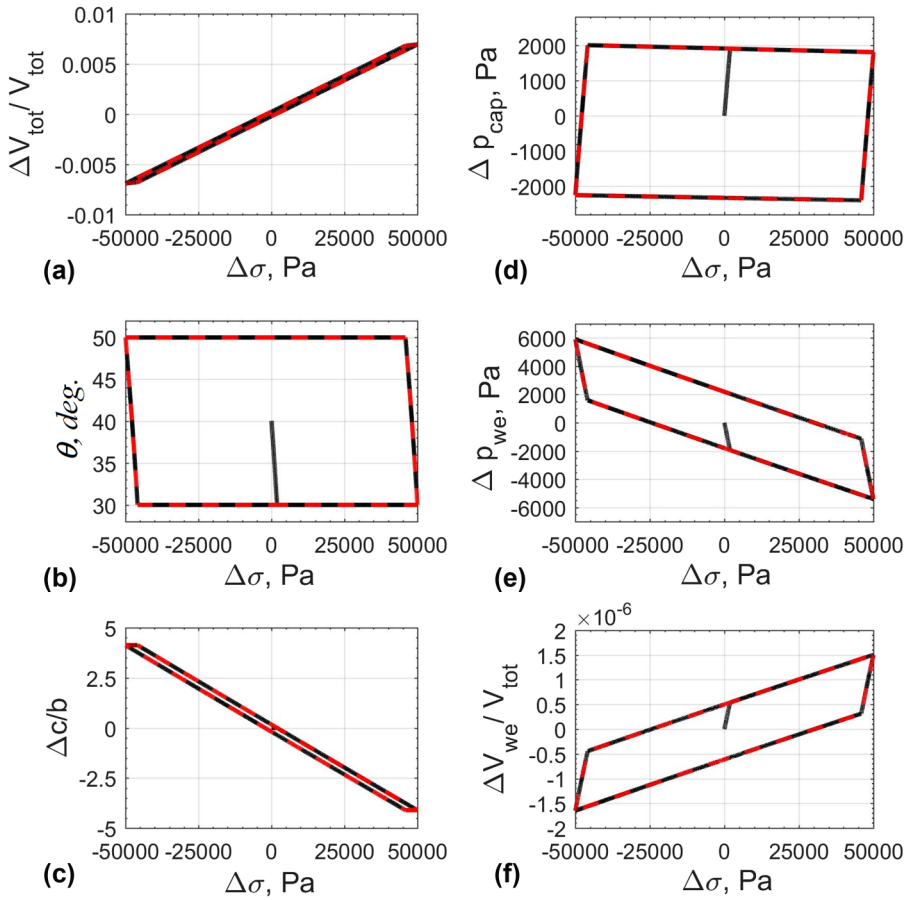

Figure 8 Effect of the hysteresis of liquid bridges on (a) changes of the crack volume (dimensionless units); (b) changes of contact angle (degrees); (c) contact line displacement (dimensionless units); (d) changes of capillary pressure (Pa); (e) changes of pressure in the wetting phase (Pa); (f) changes of the wetting phase volume inside the crack (dimensionless units). Horizontal axis shows the magnitude of transient stress (Pa). Initial (equilibrium) crack saturation is $S_{we} = 0.75$. The initial contact angle is equal to the Young's angle. Other input parameters are given in Table 1. The amplitude of the applied periodic stress perturbation ($\Delta\sigma$) is 50 kPa. Similar to Fig. 5, the first cycle ($N = 1$) is shown by a continuous black curve, while subsequent cycles are shown by a red dashed curve.

significant, depending on the choice of input parameters. Amplitudes of Δp_{cap} and Δp_{we} perturbations (Fig. 7d and 7e) are predicted to be lower than the amplitude of $\Delta\sigma$. Depending on the choice of input parameters, these amplitudes can also be higher than the amplitude of the stress perturbation.

The case when the amplitude of the applied periodic stress perturbation ($\Delta\sigma$) is 50 kPa is shown in Fig. 8(a–f). In this case, the meniscus bending is much smaller than the contact line motion, because the wave amplitude is large. The hysteresis effect is also predicted for all six independent parameters. The hysteresis effect of the crack volume (Fig. 8a) is small because the bending of interface meniscus is much smaller than the contact line motion.

Calculations of this section show that the hysteresis of liquid bridges strongly depends on the amplitude of wave-induced stress perturbation. In the next section, we explain how to relate this effect to the effective properties of the representative elementary volume (REV), such as bulk moduli and attenuation. The influence of other parameters—effective stress, wettability, crack size and frequency—is investigated in Section 4.3.

4 EFFECTIVE BULK MODULI AND ATTENUATION

4.1 Effective properties of the REV

In this section, we calculate effective properties of the REV, such as compressibility, bulk modulus and quality (attenuation) factor. The apparent compressibility of the REV (C_{REV})

can be calculated using Betti's reciprocal theorem (e.g. Walsh 1965; Mavko and Jizba 1991):

$$C_{\mathrm{REV}} = C + \frac{1}{V_{\mathrm{REV}}} \frac{\Delta V_{\mathrm{tot}}}{\Delta \sigma}, \tag{4}$$

where C is the compressibility of the solid material around a crack, V_{REV} is the volume of REV, and ΔV_{tot} is the change of total pore (crack) volume for a given stress perturbation $\Delta\sigma$. Plane-strain compressibility of the solid material around a crack is related to the Young's modulus (E) and Poisson's ratio (v) of the material:

$$C = \frac{2(1+v)(1-2v)}{E}. \tag{5}$$

The REV volume per unit length in $z-$directions, perpendicular to the plane of Fig. 4, is calculated as $V_{\mathrm{REV}} = \pi R^2$. Here, R is the radius of the REV (see Fig. 4), which can be related to the initial crack porosity, n_c, by $R = \sqrt{ab/n_c}$. The initial crack porosity is the porosity at zero effective stress. Thus, the REV volume can be calculated as follows:

$$V_{\mathrm{REV}} = \frac{\pi ab}{n_c}. \tag{6}$$

Thus, the compressibility of REV is proportional to the slope of ΔV_{tot} versus $\Delta\sigma$ curves, shown in Figs 6(a), 7(a) and 8(a). Due to hysteresis effect, we approximate this slope by the slope of the largest diagonal of the parallelogram, shown in Figs 7(a) and 8(a) or by the slope of line shown in Fig. 6(a). This choice of the slope would predict correctly the maximum strain for a given stress perturbation $\Delta\sigma$. Note here that, due to non-linear effects, the definition of REV compressibility is not unique. Zimmerman (1990) discussed that the compressibility of REV can be calculated by two different methods. The first method conserves the elastic strain, while the second method conserves the elastic wave energy. The difference between these two methods is small when the hysteresis (non-linearity) is small. In this paper, we choose the first method in the calculation of REV compressibility and the second method in the calculation of the wave energy dissipation.

The effective bulk modulus of REV (B_{REV}) is the reciprocal of REV compressibility:

$$B_{\mathrm{REV}} = \frac{1}{C_{\mathrm{REV}}}. \tag{7}$$

The elastic energy, W, per unit volume of REV is calculated using equation $W = \frac{1}{2} C_{\mathrm{REV}} \Delta\sigma^2$ (Mavko *et al.* 2009) as follows:

$$W = \frac{1}{2}\left(C\Delta\sigma + \frac{\Delta V_{\mathrm{tot}}}{V_{\mathrm{REV}}}\right)\Delta\sigma. \tag{8}$$

However, the attenuated energy (δW) per period and per unit volume of REV is proportional to the area of the parallelogram in Figs 6(a), 7(a) and 8(a). When the contact line is pinned, there is no energy attenuation due to contact line friction (Fig. 6a). In other cases (Figs 7a and 8a), the elastic wave energy is converted to the heat due to the contact line friction mechanism.

Mathematically, δW is calculated by integration of the area of the parallelogram as follows:

$$\delta W = \frac{\oint \Delta V_{\mathrm{tot}}\, \mathrm{d}\Delta\sigma}{V_{\mathrm{REV}}}, \tag{9}$$

where the integral is taken over the period of seismic wave (we consider subsequent cycles, when the hysteresis loop is established). Note here that the attenuated wave energy per cycle in equation (9) does not depend on the calculation method of REV compressibility discussed above.

The quality or attenuation factor in the fraction of energy loss per period is calculated as follows (Mavko *et al.* 2009):

$$Q = 2\pi \frac{W}{\delta W}. \tag{10}$$

Note here that the Q-factor is large when (i) δW is small or when (i) W is large. The case when δW is small ($= 0$) is shown in Fig. 6(a), while the case when W is large is shown in Fig. 8(a). The minimum value of the Q-factor is at the intermediate stage, shown in Fig. 7(a).

4.2 Voigt and Reuss bounds

It has been demonstrated that the impact of partial saturation on the bulk modulus of REV can be attributed to an effective fluid modulus of a single-phase fluid (e.g. Mavko *et al.* 2009; Papageorgiou *et al.* 2016). Mavko and Mukerji (1998) suggested that the upper and lower bounds on low-frequency seismic velocity in a partially saturated rock are controlled by Voigt and Reuss averaging equations of fluid bulk moduli. The Voigt upper bound of the effective bulk modulus of fluid is calculated by arithmetic volume average:

$$K_{\mathrm{fl}} = K_{\mathrm{we}} S_{\mathrm{we}} + K_{\mathrm{nw}}(1 - S_{\mathrm{we}}), \tag{11}$$

while the Reuss lower bound is calculated by harmonic volume average:

$$\frac{1}{K_{\mathrm{fl}}} = \frac{S_{\mathrm{we}}}{K_{\mathrm{we}}} + \frac{1 - S_{\mathrm{we}}}{K_{\mathrm{nw}}}. \tag{12}$$

Brie *et al.* (1995) suggested the following empirical mixing law for liquids and gases, based on the experimental testing of partially saturated sandstone:

$$K_{\mathrm{fl}} = (K_{\mathrm{we}} - K_{\mathrm{nw}})\ (S_{\mathrm{we}})^{e} + K_{\mathrm{nw}}. \tag{13}$$

Here, the gas is always the non-wetting phase relative to most liquids, except mercury. e is the empirical constant in the above equation with a typical value equal to 3. Brie empirical correlation recovers the Voigt upper bound when $e = 1$ and predicts values close to the Reuss lower bound when $e \sim 50$. Thus, Brie correlation predicts values between Voigt and Reuss bounds, depending on the empirical e parameter.

The Voigt and Reuss bounds are also known as isostrain and isostress averages, respectively, because they give the ratio of average stress to average strain when all constituents are assumed to have either the same strain or the same stress. The upper and lower bounds, suggested by Mavko and Mukerji (1998), consider only different averaging methods of fluid moduli and do not consider any solid–fluid and fluid–fluid interactions, which can potentially lead to either weakening or strengthening effects of the effective fluid moduli.

In this paper, we compare results of our model with predictions using the upper and lower bounds for the fluid modulus. To do so, we need to derive the equation for REV compressibility, considering that the crack is fully saturated by a single-phase fluid with effective properties. In this case, the expression for the REV compressibility is calculated as follows (see Appendix A.5):

$$C_{\mathrm{REV}} = \frac{2\,(1+v)\,(1-2v)}{E} + \frac{n_c}{p_{\mathrm{cl}}}\,\frac{p_{\mathrm{cl}} + \sigma + p_{\mathrm{fl}}}{p_{\mathrm{cl}} + \sigma + p_{\mathrm{fl}} + K_{\mathrm{fl}}}. \tag{14}$$

There are two uncertainties in this equation: effective fluid pressure (p_{fl}) and effective fluid bulk modulus (K_{fl}). Bounds for the effective fluid bulk modulus are discussed above. Due to capillary pressure, the effective fluid pressure is not well defined. Some of the researchers suggested to use volumetric averaging for the effective fluid pressure (e.g. Santos *et al.* 1990; Papageorgiou *et al.* 2016).

$$p_{\mathrm{fl}} = p_{\mathrm{we}} + p_{\mathrm{cap}}\,(1 - S_{\mathrm{we}})\,. \tag{15}$$

In our previous publication (Rozhko 2016), we demonstrated that the volume of a partially saturated crack is controlled by the effective stress in which fluid pressure is calculated by the above equation.

Next, by substituting equations (11) and (15) into equation (14), we calculate the Voigt upper bound for the effective compressibility of REV. The Reuss lower bound is calculated in a similar way.

Table 2 Table shows which input parameters for cases 2–4 are different from case 1 (see Table 1)

Case 2 (Frequency effect)	
Advancing contact angle for wetting phase (θ_a)	54°
Receding contact angle for wetting phase (θ_r)	26°
Case 3 (Stress effect)	
Effective stress ($\sigma + p_{\mathrm{we}}$)	−15 MPa
Case 4 (Wettability effect)	
Advancing contact angle for wetting phase (θ_a)	5°
Receding contact angle for wetting phase (θ_r)	3°
Major semi-axis (a)	10^{-4} m

4.3 Numerical results

In this section, we present numerical results for bulk moduli (B_{REV}) and seismic attenuation ($1/Q$), calculated for a representative elementary volume with a partially saturated crack. We will investigate the role of different input parameters, given in Tables 1 and 2. In Fig. 9 (case 1) we investigate the effect of wave amplitude and liquid saturation (liquid/gas system) on bulk moduli and seismic attenuation.

Figure 9(a) shows that the bulk modulus of REV is highly sensitive to the wave amplitude, shown on the colour scale. Higher bulk moduli correspond to smaller wave amplitude. It is consistent with laboratory measurements (e.g. Iwasaki, Tatsuoka and Takagi 1978; Tutuncu *et al.* 1998; Mashinskii 2004; Nourifard and Lebedev 2018). Grey and black curves in Fig. 9(a) show the Voigt and Reuss upper and lower bounds, calculated in the previous section. The upper Voigt bound, calculated in Fig. 9(a), reaches its nearly maximum value at a few percentage of water saturation. One may argue that this behaviour is not realistic. In this paper, we consider an REV with a single isolated crack, and this upper bound is correct for the case we are considering. Natural rocks contain many cracks of different sizes and aspect ratios plus matrix porosity. Thus, for natural rocks the Voigt bound will not be that steep at small saturations, due to averaging over different cracks and pores. When the wave amplitude is large, the bulk modulus is close to the Reuss bound (Fig. 9a), while the bulk modulus for small wave amplitudes shows intermediate values between the Voigt and Reuss bound values. This intermediate value is sometimes referred in the literature as the Voigt–Reuss–Hill average (e.g. Mavko *et al.* 2009). Note here that the Brie empirical correlation also predicts intermediate values between Voigt and Reuss bounds values, as discussed in Section 4.2. These intermediate values are predicted in the limit when the wave amplitude is small, and the contact line is pinned. In this case, the interface meniscus restricts the

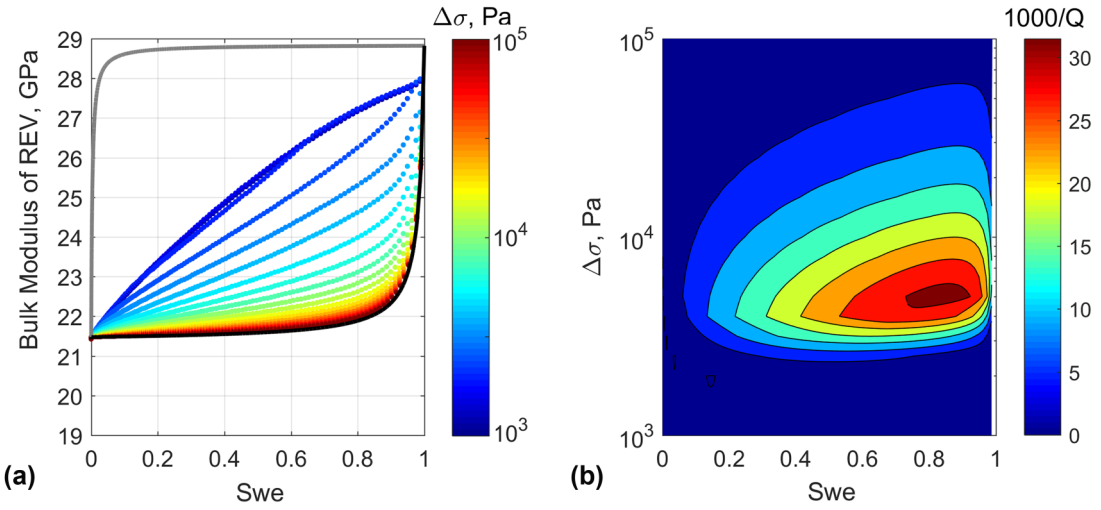

Figure 9 (a) Bulk modulus of REV versus wetting phase saturation, calculated for different magnitudes of wave-induced stress perturbation, shown on the colour scale. Grey and black curves show the Voigt and Reuss upper and lower bounds. (b) Attenuation $1000/Q$ factor is shown on the colour scale, as a function of wave-induced stress perturbation magnitude and wetting phase saturation, shown on abscissa and ordinate, respectively. See Table 1 for input parameters for case 1.

relative motion of fluids during wave-induced two-phase fluid flow. Figure 9(b) shows seismic attenuation $1000/Q$-factor as a function of wave-induced stress perturbation magnitude and wetting phase saturation. When the wave amplitude is small $\Delta\sigma = 1$ kPa, there is no attenuation of seismic energy, because the contact line is pinned. When the wave amplitude is large enough, the contact line will slip, causing the dissipation of the wave energy to the heat due to the contact line friction mechanism. Thus, the energy loss increases with wave amplitude; however, the attenuation factor depends on the ratio between the wave energy and attenuated energy, according to equation (10). Maximum of $1/Q$ will be achieved at certain stress amplitude as shown in Fig. 9(b), which also depends on the saturation.

In Fig. 10 (case 2) we consider the effect of frequency increase, which we relate in our model to the change of contact angle hysteresis (Table 2), while other input parameters for case 2 are the same as for case 1. In Section 2, we discussed that the effect of frequency change can be related to the effect of the contact angle hysteresis change, according to experimental observations. The exact relation between frequency and contact angles is complex, because it also depends on the wave amplitude (Section 2). Thus, in calculations of Fig. 10, we focus only on the effect of the contact angle hysteresis change. Figure 10(a) shows that the increase of the contact angle hysteresis increases pinning forces for interface menisci. This results in increase of bulk moduli for given wave amplitude, as can be seen by comparing Figs 9(a) and 10(a). Figures 9(b) and 10(b) show that the increase of the contact angle hysteresis shifts the attenuation peak towards higher stress amplitudes, while the maximum value of $1/Q$ does not change significantly for selected input parameters. Since the attenuation peak has shifted with the frequency on the colour map of Figs 9(b) and 10(b), it implies that the attenuation can either increase or decrease with frequency (in the low frequency range). Experimental results of Moerig *et al.* (1996) confirmed that seismic attenuation can either increase or decrease with frequency in the low frequency range from 0.001 to 5 Hz, depending on chemical treatment of the crack surface. Note here that standard theories would predict a linear increase of attenuation with frequency, in the low frequency range due to viscous dissipation in the bulk (Pride *et al.* 2004; Mavko *et al.* 2009; Müller *et al.* 2010). Our model predicts seismic attenuation due to a contact line friction mechanism, which occurs at the contact line location and is responsible for more complex dependence of attenuation on the frequency, as observed by Moerig *et al.* (1996).

In Fig. 11 (case 3) we study the effect of stress increase, considering that the initial p_{we} is the same as in all previous cases. Note here that fluid bulk moduli, surface tension and contact angles are functions of fluid pressure, which must be taken into account when the initial fluid pressure is different, but the effective stress is the same. Thus, in a general case when both total stresses and pore pressure change, the

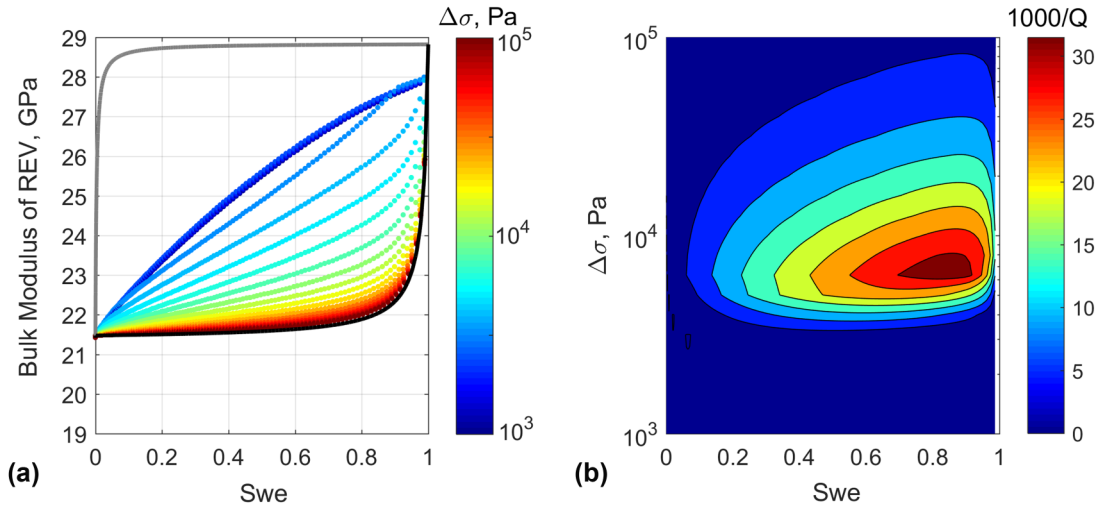

Figure 10 (a) Bulk modulus of REV versus wetting phase saturation, calculated for different magnitudes of wave-induced stress perturbation, shown on the colour scale. Grey and black curves show the Voigt and Reuss upper and lower bounds. (b) Attenuation $1000/Q$ factor is shown on the colour scale, as a function of wave-induced stress perturbation magnitude and wetting phase saturation, shown on abscissa and ordinate, respectively. See Tables 1 and 2 for input parameters for case 2 (frequency effect).

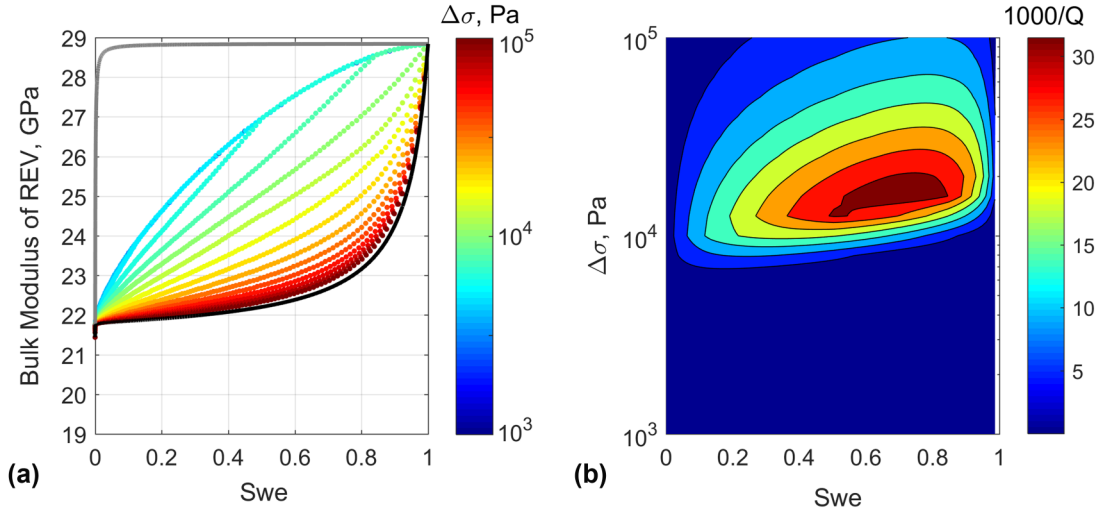

Figure 11 (a) Bulk modulus of REV versus wetting phase saturation, calculated for different magnitudes of wave-induced stress perturbation, shown on the colour scale. Grey and black curves show the Voigt and Reuss upper and lower bounds. (b) Attenuation $1000/Q$ factor is shown on the colour scale, as a function of wave-induced stress perturbation magnitude and wetting phase saturation, shown on abscissa and ordinate, respectively. See Tables 1 and 2 for input parameters for case 3 (stress effect).

dependence on the effective stress would be more complex, because the aforesaid parameters will also change with the fluid pressure. Figure 11(a) shows that the increase of total confining stress causes an increase in bulk moduli, as one can see by comparing with Fig. 9(a). Furthermore, when the bulk saturation is low ($S_{we} \to 1$), the bulk moduli for small wave amplitudes follow an upper Voigt bound. Figures 9(b) and 11(b) show that the increase in total stress shifts the attenuation peak towards higher stress amplitudes and the maximum value of $1/Q$ slightly increases for selected input parameters.

In Fig. 12 (case 4) we study the effect of wettability increase, which we relate to the decrease of contact angles, according to Table 2. Furthermore, to amplify the surface phenomenon effects, we consider the smaller length of the crack having the same aspect ratio as in case 1. The upper and lower bounds, proposed by Mavko and Mukerji (1998), consider only different averaging methods of fluid

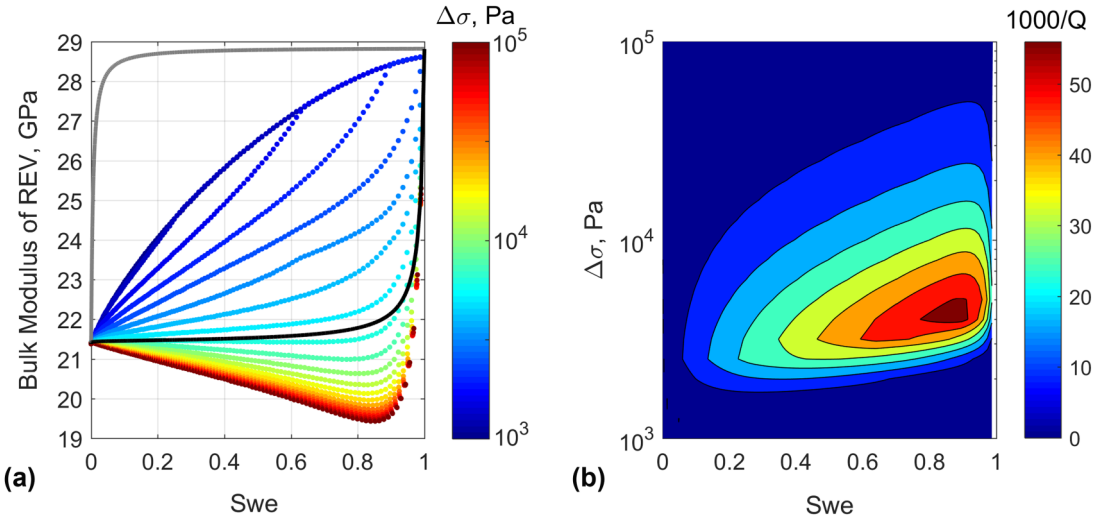

Figure 12 (a) Bulk modulus of REV versus wetting phase saturation, calculated for different magnitudes of wave-induced stress perturbation, shown on the colour scale. Grey and black curves show the Voigt and Reuss upper and lower bounds. (b) Attenuation $1000/Q$ factor is shown on the colour scale, as a function of wave-induced stress perturbation magnitude and wetting phase saturation, shown on abscissa and ordinate, respectively. See Tables 1 and 2 for input parameters for case 4 (wettability effect).

moduli and do not consider any solid–fluid and fluid–fluid interactions. Thus, due to interactions at solid, liquid and gas interfaces, we may expect the deviation from Reuss and Voigt bounds. Figure 12(a) shows that such deviation (weakening) is possible due to surface phenomenon effects. Figure 12(b) shows that the amplitude of seismic attenuation (maximum value) increases significantly, compared with cases 1–3. Note the difference in colour scales between Fig. 12(b) and Figs 9(b)–11(b). The weakening effect of pore liquids is widely reported in the literature (e.g. see Li *et al.* 2017 for review). Although many water-weakening mechanisms are proposed in the literature, Murphy (1984) and Murphy *et al.* (1986) suggested the experiment to demonstrate that water-weakening effect takes place even in unconsolidated sandstones, where other weakening mechanisms (swelling of clay cement, osmotic suction and dissolution and dissolution of calcite) are excluded. Murphy (1984) and Murphy *et al.* (1986) proposed a model that explains the frame modulus reduction in sedimentary rocks by adsorption of liquid on a grain contact. In contrast, our model suggests the frame modulus reduction due to adsorption at the crack surface. Zimmerman (1990) suggested that in granular materials some pores are very thin "crack-like" that exist along grain boundaries. Furthermore, Zimmerman (1990) argued that even though the crack porosity can be a small fraction of the total porosity, "crack-like" pores may have a significant effect on the compressibility of sandstones. Thus, the contact angle hysteresis can be important even for granular materials, in which the liquid is adsorbed in crack-like pores along grain boundaries. In the next section, we discuss adsorption–desorption effects inside a crack.

4.4 Drainage-imbibition hysteresis

Laboratory data suggest that seismic properties of sandstone are highly sensitive to the saturation history. Knight and Nolen-Hoeksema (1990) reported experimental data for the P-wave velocity of a tight gas sandstone measured as water saturation was first increased (imbibition) and then decreased (drainage). They observed that P-wave velocity during drainage is larger than during imbibition. Similar conclusions were observed by other researchers, for example, by Zhang *et al.* (2015), who conducted P-wave velocity and its attenuation measurements on low-permeability sandstone during drainage (CO_2 injection) and imbibition (brine injection), as shown in Fig 13(a) and 13(b). Furthermore, they observed that seismic attenuation during imbibition is larger than during drainage, as shown in Fig. 13(b). Different explanations for the hysteresis of acoustic properties are proposed in the literature. Patch-size-dependent models are a common approach to explain hysteresis in the geophysical literature (Zhang *et al.* 2015; Mavko *et al.* 2009). Other researchers argued that effective bulk moduli of fluid are dependent on the pore-scale capillarity and on the interface area between immiscible fluids (Papageorgiou *et al.* 2016; Knight *et al.* 2010).

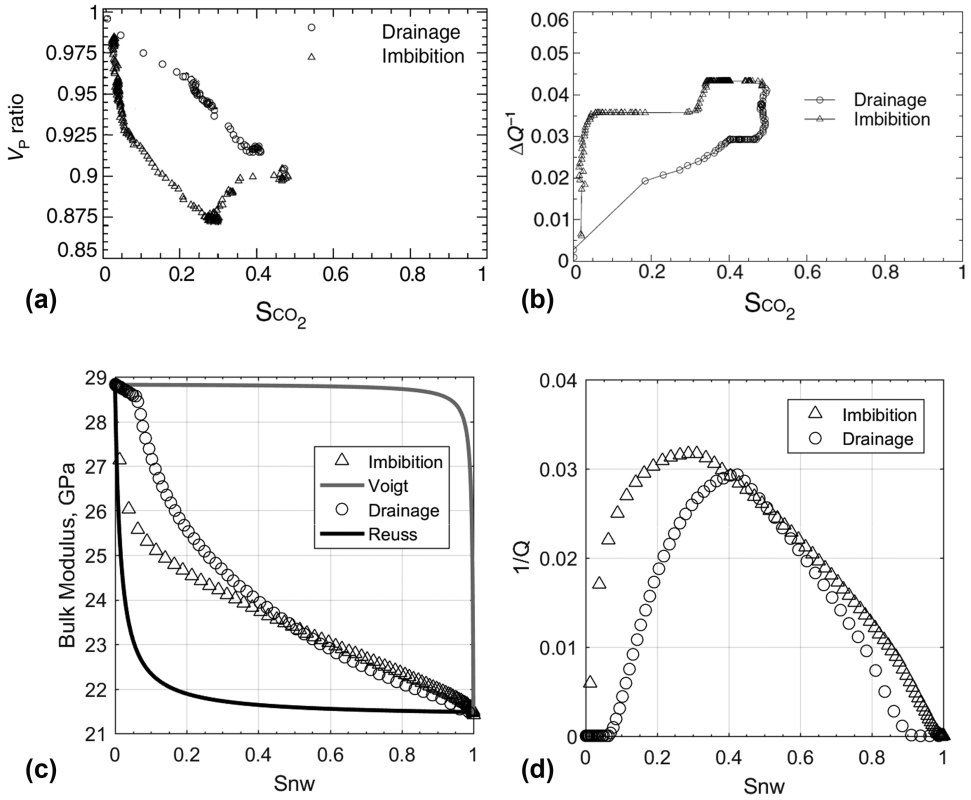

Figure 13 (a, b) Laboratory measurements of P-wave velocity and its attenuation on low-permeability sandstone during drainage (CO_2 injection) and imbibition (brine injection) (modified after Zhang *et al.* 2015). (c, d) Calculated bulk moduli and attenuation hysteresis during drainage and imbibition, see Table 1 for input parameters and Fig. 14 for the "inkbottle" effect during drainage and imbibition. Horizontal scale in (a) and (b) shows gas saturation of the core sample, while in (c) and (d) shows gas saturation of the crack. Both experimental and numerical results predict higher velocity and bulk moduli during drainage and lower attenuation during drainage at gas saturations below 50%.

In order to better understand how the pore-scale capillarity affects the interface area and how this is related to our liquid-bridge hysteresis model, let us consider the pore-blocking effect. We refer to the pore-blocking effect, which is one of the earliest concepts used to describe the hysteresis of physical properties during drainage and imbibition experiments (Kraemer 1931; McBain 1935; Libby and Monson 2004; Coussy 2011). This concept can be described in terms of a pore geometry that has come to be known as the 'inkbottle'. This geometry consists of a larger pore space in contact with a bulk vapour through one or more narrower pore spaces or 'necks', as shown schematically in Fig. 14. The classical explanation for the phenomenon of hysteresis in such pores assumes that desorption (drainage) from the larger cavity is retarded by the presence of liquid-saturated regions in the smaller necks. Desorption (drainage) from the larger cavity occurs when all the channels connecting it to the bulk region are empty, as shown schematically in Fig. 14(a). Fluid in the larger cavity is blocked from evaporating, even below pressures low enough for it to be thermodynamically unstable. This implies the possibility of the energetically unfavourable distribution of fluids during drainage. During adsorption (imbibition), small necks are filled first by capillary

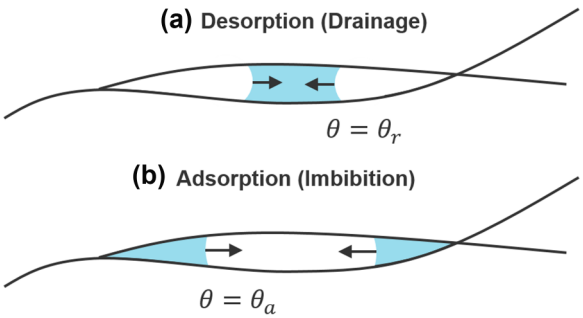

Figure 14 Drainage/imbibition hysteresis due to "inkbottle effect" in the crack-like pore. (a) Desorption, brine is in centre (wide) part. (b) Adsorption, air is in centre (wide) part. In this geometry, open area of the crack is in contact with a bulk vapour through permeable tips of the open crack.

condensation mechanisms (Fig. 14b). In addition to the pore-blocking and patch-size effects, there are also other hysteresis mechanisms suggested in the literature: contact angles hysteresis, trapping of air bubble, clay swelling and dissolution and precipitation of minerals. Note here that the "inkbottle" concept is flexible enough to include contact angles hysteresis and trapping of air bubble effects into account. For example, Fig. 14 shows that contact angles during drainage and imbibition are different. However, the trapping of air bubbles can be modelled by considering the adsorption process (Fig. 14b), which started on the top of an unfinished desorption process (Fig. 14a).

In this paper, we derived equations (see Appendix) for the case when the wetting liquid phase occupies thin parts of the crack (tips), while the non-wetting gas phase occupies wide parts of the crack (centre). Such distribution of fluids is energetically favourable and corresponds to adsorption (imbibition) case, shown in Fig. 14(b). Our equations, after small modifications, are also applicable to the case when the wetting fluid phase is in the central part of the crack, while tips of the crack are occupied by air. The following modifications of input and output parameters should be made for this case: $K_{we} \rightarrow K_{nw}$, $K_{nw} \rightarrow K_{we}$, $\theta_a \rightarrow \pi - \theta_r$, $\theta_r \rightarrow \pi - \theta_a$, $p_{we} \rightarrow p_{nw}$, $p_{nw} \rightarrow p_{we}$, $p_{cap} \rightarrow -p_{cap}$ and $S_{we} \rightarrow 1 - S_{we}$.

Figure 13(c) and 13(d) shows calculated bulk modulus and seismic attenuation during drainage and imbibition. Input parameters for calculations are given in Table 1 and calculated for wave-induced stress perturbation amplitude of $\Delta\sigma = 4$ kPa. Calculations in Fig. 13(c) show that bulk modulus during drainage is higher than during imbibition for gas saturation $S_{nw} < 0.5$. A similar trend was observed for P-wave velocity shown in Fig. 13(a). Calculations in Fig. 13(d) show that the seismic attenuation factor during drainage is smaller than during imbibition for gas saturation $S_{nw} < 0.5$. A similar trend was observed in the lab as shown in Fig. 13(b). Thus, our model suggests that the hysteresis of seismic properties during drainage and imbibition is controlled by pore-scale capillarity effects during absorption and desorption.

5 DISCUSSIONS

In this paper, we investigated the hysteresis of liquid bridges effect in an isolated partially saturated crack. For simplicity, we focused only on interface phenomenon effects by considering a uniform far-field compressive stress and uniform wave-induced stress perturbations. Natural rocks contain many cracks of different length and aspect ratios. Furthermore, directions of preferred crack orientation, *in situ* stress directions and the wave propagation direction could be different. These will introduce anisotropy into the wave response. The current model can be extended towards this more complex situation, combining both interface phenomena and anisotropy effects. In our model, we approximated the crack by smoothed-wall elliptical geometry. Cracks in natural rocks are not smoothed wall. The roughness of the crack surface will affect advancing and receding contact angles, which will depend on the contact line location, that is, $\theta_a(c)$ and $\theta_r(c)$. In our calculations, we consider θ_a and θ_r to be independent on the contact line locations; however, the incremental approach, developed in this paper, allows one to address this more complex situation, if $\theta_a(c)$ and $\theta_r(c)$ are known. A theoretical model shows that seismic velocities of the partially saturated rock depends not only on the pore pressure and gas saturation, but also on the amplitude (and frequency) of the seismic wave. These can be used to run acoustic logs and seismic surveys not only in the multi-frequency range, but also in the multi-amplitude range. This methodology will allow one to extract more information from seismic data, considering both the frequency and amplitude effects. Where the amplitude effects were not analysed before, acquisition of additional data (the multi-amplitude data) will allow the interpretation of seismic velocities and acoustic logs both for pore pressure and gas saturation using a new rock physics model. The new model considers a physical process called 'liquid bridge hysteresis', which was not considered before by a rock physics community.

The model developed in this paper is applicable for the low frequency limit (seismic frequencies) when capillary forces dominate over viscous forces during wave-induced two-phase fluid flow. Wave-induced viscous forces are proportional to gradients of pore pressure, while in the low frequency limit, gradients of pore pressure are zero; thus, viscous forces are also zero, causing zero seismic attenuation (e.g. Mavko *et al.* 2009). However, the change of the capillary forces, caused by the deformation of liquid bridges, is not equal to zero in the low frequency limit, causing a non-negligible seismic attenuation. Thus, the wave-induced two-phase fluid flow in the low frequency is dominated by capillary forces, which are typically neglected in Biot–Gassmann's models (e.g. Mavko *et al.* 2009). To estimate the effect produced by viscous forces at seismic frequency, we can apply results of Mavko and Nur (1979) who considered viscous dissipations in a partially saturated crack. Calculations of Mavko and Nur (1979) show that for the crack porosity of $n_c = 2 \times 10^{-4}$ and crack aspect ratio of 10^{-3}, the attenuation factor, calculated for Boise sandstone at frequency = 1.6 Hz and uniform 50% water saturation is $Q^{-1} = 4.2 \times 10^{-5}$. Calculations presented in our

paper, using elastic parameters, typical for Boise sandstone and using the same crack porosity, aspect ratio and water saturation, show that (Figs 9b–12b) typical values for Q^{-1} are about two orders of magnitude higher than Mavko and Nur (1979) results. Furthermore, Mavko and Nur (1979) predicted a liner scaling of the Q^{-1} with the frequency, in the low frequency limit. It implies that we can estimate the frequency range where the contact line friction dominates over viscous dissipation. Simple calculations suggest that the contact line friction may dominate viscous dissipations in Boise sandstone at frequencies below 200 Hz, that is, at seismic frequencies. Contact line frictional dissipations depend also on the wave amplitude. If the wave amplitude is small and the contact line is pinned, then dissipations caused by the contact line frictions are zero. In this case, when the contact line is pinned, viscous dissipations will dominate seismic attenuation, while the surface tension will still affect the effective bulk modulus of fluid, by restricting the relative motion of fluids during wave-induced two-phase fluid flow.

In this paper, we demonstrated that a negligibly small fraction of free gas ($\approx n_c S_{nw} < 0.01\%$ of the total sample volume) could be enough to cause seismic attenuation in the low frequency limit due to the hysteresis of liquid bridges. At the same time, several authors discussed that it is extremely difficult to achieve 100% saturation of the rock sample, especially if the rock sample is tight (e.g. Murphy 1984; Verwer *et al.* 2010; Li *et al.* 2017). Even after applying different advanced saturation techniques, there might be some pores that are not completely saturated. For example, Li *et al.* (2017) argued that the maximum water saturation, achieved in tight sandstone, was $\sim 98\%$. Thus, our results can be applied to analyse experimental data, conducted on an almost fully saturated rock. At 100% saturation, this effect, however, will disappear if there is only one saturating phase.

To conclude, it is difficult to apply this model to the published laboratory data, because many input parameters of the model are not reported in the published literature. For example, our model depends on the wettability towards different saturating fluids, described by the advancing and receding contact angles. Also, the applied wave amplitude could be different in different experiments. These details are not presented in the published literature, because it is not common yet to pay attention to interface phenomenon effects. However, we can present examples of published laboratory data, showing that a non-zero seismic attenuation at zero frequency limit depends on the pore fluid and this cannot be explained by diffusion-based models. Laboratory data presented by Spencer and Shine (2016) showed that it is not possible to explain the fluid effect on small seismic attenuation at low frequency limit using the Cole–Cole fit. The Cole–Cole fit is based on the permeability and viscosity scaling and thus predicting zero attenuation at low frequency limit. The amplitude of P-wave attenuation in the low frequency limit, reported by Spencer and Shine (2016) for different pore fluids in sandstone samples, was around $Q^{-1} \sim 0.005$, while the reported precision of laboratory measurements was around $\Delta Q^{-1} \sim \pm 0.002$. Thus, the observed fluid effect on non-zero attenuation at zero frequency limit could be related to the contact line friction; however, this interpretation is not unique, because it can also be related to the frequency- and amplitude-independent plastic yielding mechanism (Yarushina and Podladtchikov 2010). To differentiate between these two possible interpretations, it is important to investigate the effect of wave amplitude on seismic attenuation in the low frequency limit.

6 CONCLUSIONS

In this paper, we investigated the effect of the hysteresis of liquid bridges on seismic attenuation and bulk moduli of a partially saturated rock. Our model considers physicochemical interactions on interfaces between liquid–gas, liquid–solid and gas–solid. The role of these interfaces is not studied by classical rock physics models, which are based on the classical theory of poroelasticity and mixing theories. Mixing theories consider different methods of volumetric averaging (of liquids, gas, and solid) and do not consider interactions between three phases. Understanding of this interaction is important to explain certain experimental observations, which cannot be understood using classical models, such as Biot, Gassmann and squirt flow.

Using our model, we demonstrated the following:

- The Brie-like behaviour for the effective bulk modulus of pore fluid is controlled by the hysteresis of liquid bridges, which is sensitive to the following parameters: the wave amplitude, elastic properties of the solid and fluids, crack geometry (length and aspect ratio), effective confining stress, rock wettability (advancing and receding contact angles) and surface tension between immiscible fluids.
- The effect of drainage and imbibition on dynamic bulk moduli and attenuation are explained by the inkbottle (pore-blocking) effect in the partially saturated crack. This effect suggests that the saturation distribution inside the crack is different during drainage (gas injection) and during imbibition (water injection). This will affect the hysteresis of liquid bridges inside the partially saturated crack.

- Wettability has a significant control on the water-weakening effect, which can be explained by physicochemical interactions on interfaces between three phases.
- The role of immiscible fluids on the low-frequency seismic attenuation is rather non-trivial; it can either increase or decrease with frequency (in the range from 0.001 to 5 Hz). The attenuation mechanism in this frequency range can be dominated by the contact line friction, rather than by viscous dissipation in the bulk.
- The model predicts the residual changes of fluid pressure, saturation and crack porosity caused by the passage of seismic waves.

Closed-form analytical solutions are proposed for the description of the hysteresis of liquid bridges in a representative elementary volume (REV) containing a crack that is partially saturated with two immiscible fluids. The model is sensitive towards the following input parameters: effective stress, wave amplitude (wave-induced perturbation of stress), elastic moduli of the rock around a crack, advancing and receding contact angles, surface tension, bulk moduli of liquid and gas, saturation degree, crack porosity, crack length and aspect ratio. In the next step of our research, we will apply the model for shallow gas exploration and CO_2 monitoring.

ACKNOWLEDGEMENTS

I am grateful to the anonymous reviewers, Giorgos Papageorgiou and to the associate editor, Tobias Mueller, who helped to improve the manuscript. Andreas Bauer, Anne-Kari Furre Anne-Kari Furre and William Waite are acknowledged for discussions on early stages.

REFERENCES

Barenblatt G.I., Entov V.M. and Ryzhik V.M. 1990. *Theory of fluid flows through natural rocks*. Kluwer Academic Publishers.

Bonn D., Eggers J., Indekeu J., Meunier J. and Rolley E. 2009. Wetting and spreading. *Reviews of modern physics*, **81**, 739.

Bormashenko E.Y. 2013a. Wetting of real surfaces (Vol. **19**). Walter de Gruyter.

Bormashenko E. 2013b. Wetting of real solid surfaces: new glance on well-known problems. *Colloid and Polymer Science* **291**, 339–342.

Brie A., Pampuri F., Marsala A.F. and Meazza O. 1995 (January). Shear sonic interpretation in gas-bearing sands. In SPE Annual Technical Conference and Exhibition. Society of Petroleum Engineers.

Broadhead M.K. 2012. Effect of contact line motion on QP and QS for partially saturated rocks. In SEG Technical Program Expanded Abstracts 2012 (pp. 1–6). Society of Exploration Geophysicists.

Brunner W. and Spetzler H.A. 2001. Observations of time-dependent meniscus behavior with implications for seismic attenuation in three-phase systems. *Geophysical Research Letters* **28**, 1867–1870.

Chen H., Amirfazli A. and Tang T. 2013. Modeling liquid bridge between surfaces with contact angle hysteresis. *Langmuir*, **29**, 3310–3319.

Chibowski E. 2008. Surface free energy of sulfur—Revisited I. Yellow and orange samples solidified against glass surface. *Journal of Colloid and Interface Science* **319**, 505–513.

Coussy O. 2011. *Mechanics and physics of porous solids*. John Wiley & Sons.

De Gennes P.G., Brochard-Wyart F. and Quéré D. 2013. *Capillarity and wetting phenomena: drops, bubbles, pearls, waves*. Springer Science & Business Media.

De Souza E.J., Gao L., McCarthy T.J., Arzt E. and Crosby A.J. 2008. Effect of contact angle hysteresis on the measurement of capillary forces. *Langmuir* **24**, 1391–1396.

Ethington E.F. 1990. Interfacial contact angle measurements of water, mercury, and 20 organic liquids on quartz, calcite, biotite, and Camontmorillonite substrates (No. 90-409). US Geological Survey.

Fredlund D.G., Rahardjo H. and Fredlund M.D. 2012. *Unsaturated soil mechanics in engineering practice*. John Wiley & Sons.

Gassmann F. 1951. Uber die elastizitat poroser medien. *Vierteljahrsschrift der Naturforschenden Gesellschaft in Zurich* **96**, 1–23.

Hudson J.A. 1988. Seismic wave propagation through material containing partially saturated cracks. *Geophysical Journal International* **92**, 33–37.

Iwasaki T., Tatsuoka F. and Takagi Y. 1978. Shear moduli of sands under cyclic torsional shear loading. *Soils and Foundations* **18**, 39–56.

Joule J.P. 1851 (January). On the mechanical equivalent of heat. In Abstracts of the Papers Communicated to the Royal Society of London (Vol. **5**, p. 839). The Royal Society.

Knight R. and Nolen-Hoeksema R. 1990. A laboratory study of the dependence of elastic wave velocities on pore scale fluid distribution. *Geophysical Research Letters* **17**, 1529–1532.

Knight R., Pyrak-Nolte L.J., Slater L., Atekwana E., Endres A., Geller J., et al. 2010. Geophysics at the interface: response of geophysical properties to solid-fluid, fluid-fluid, and solid-solid interfaces. *Reviews of Geophysics* **48**, RG4002 .

Kraemer E.O. 1931. *A Treatise on Physical Chemistry* (ed H.S. Taylor). D. Van Nostrand Company, New York.

Lauga E., Brenner M. and Stone H. 2007. Microfluidics: the no-slip boundary condition. In *Springer Handbook of Experimental Fluid Mechanics* (pp. 1219–1240). Springer, Berlin, Heidelberg.

Lavrentiev M.A. and Shabbat B.V. 1973. *Methods of the Theory of Complex Variable Functions*. Nauka, Moscow.

Li D., Wei J., Di B., Ding P. and Shuai D. 2017. The effect of fluid saturation on the dynamic shear modulus of tight sandstones. *Journal of Geophysics and Engineering* **14**, 1072.

Libby B. and Monson P.A. 2004. Adsorption/desorption hysteresis in inkbottle pores: a density functional theory and Monte Carlo simulation study. *Langmuir* **20**, 4289–4294.

Manga M., Beresnev I., Brodsky E.E., Elkhoury J.E., Elsworth D., Ingebritsen S.E., ... & Wang C.Y. 2012. Changes in permeability

caused by transient stresses: field observations, experiments, and mechanisms. *Reviews of Geophysics* **50**, RG2004.

Mashinskii E.I. 2004. Variants of the strain-amplitude dependence of elastic wave velocities in rocks under pressure. *Journal of Geophysics and Engineering* **1**, 295.

Mavko G. and Jizba D. 1991. Estimating grain-scale fluid effects on velocity dispersion in rocks. *Geophysics* **56**, 1940–1949.

Mavko G. and Mukerji T. 1998. Bounds on low-frequency seismic velocities in partially saturated rocks. *Geophysics* **63**, 918–924.

Mavko G., Mukerji T. and Dvorkin J. 2009. *The Rock Physics Handbook: Tools for Seismic Analysis of Porous Media*. Cambridge University Press.

Mavko G.M. and Nur A. 1979. Wave attenuation in partially saturated rocks. *Geophysics* **44**, 161–178.

McBain J.W. 1935. An explanation of hysteresis in the hydration and dehydration of gels. *Journal of the American Chemical Society* **57**, 699–700.

Miksis M.J. 1988. Effects of contact line movement on the dissipation of waves in partially saturated rocks. *Journal of Geophysical Research: Solid Earth* **93**, 6624–6634.

Murphy W.F. 1984. Acoustic measures of partial gas saturation in tight sandstones. *Journal of Geophysical Research: Solid Earth* **89**, 11549–11559.

Murphy W.F. III, Winkler K.W. and Kleinberg R.L. 1986. Acoustic relaxation in sedimentary rocks: dependence on grain contacts and fluid saturation. *Geophysics* **51**, 757–766.

Muskhelishvili N.I. 1977. *Some Basic Problems of the Mathematical Theory of Elasticity*. Springer, Berlin.

Müller T.M., Gurevich B. and Lebedev M. 2010. Seismic wave attenuation and dispersion resulting from wave-induced flow in porous rocks—A review. *Geophysics* **75**, 75A147–75A164.

Moerig R., Waite W.F., Boyd O.S., Getting I.C. and Spetzler H.A. 1996. Seismic attenuation in artificial glass cracks: physical and physicochemical effects of fluids. *Geophysical Research Letters* **23**, 2053–2056.

Nourifard N. and Lebedev M. 2018. Research note: the effect of strain amplitude produced by ultrasonic waves on its velocity. *Geophysical Prospecting*.

Papageorgiou G., Amalokwu K. and Chapman M. 2016. Theoretical derivation of a Brie-like fluid mixing law. *Geophysical Prospecting* **64**, 1048–1053.

Pride S.R., Berryman J.G. and Harris J.M. 2004. Seismic attenuation due to wave-induced flow. *Journal of Geophysical Research: Solid Earth* **109**, B01201.

Pruess K. and Tsang Y.W. 1990. On two-phase relative permeability and capillary pressure of rough-walled rock fractures. *Water Resources Research* **26**, 1915–1926.

Qi Q., Müller T.M., Gurevich B., Lopes S., Lebedev M. and Caspari E. 2014a. Quantifying the effect of capillarity on attenuation and dispersion in patchy-saturated rocks. *Geophysics* **79**, WB35–WB50.

Qi Q., Müller T.M. and Rubino J.G. 2014b. Seismic attenuation: effects of interfacial impedance on wave-induced pressure diffusion. *Geophysical Journal International* **199**, 1677–1681.

Ren W. and E W. 2007. Boundary conditions for the moving contact line problem. *Physics of Fluids* **19**, 022101.

Rozhko A.Y. 2016. Two-phase fluid-flow modeling in a dilatant crack-like pathway. *Journal of Petroleum Science and Engineering* **146**, 1158–1172.

Rozhko A.Y. and A. Bauer 2018. Contact line friction and surface tension effects on seismic attenuation and effective bulk moduli in rock with a partially-saturated crack. *Geophysical Prospecting*.

Santos J.E., Douglas J. Jr, Corberó J. and Lovera O.M. 1990. A model for wave propagation in a porous medium saturated by a two-phase fluid. *The Journal of the Acoustical Society of America* **87**, 1439–1448.

Shi Z., Zhang Y., Liu M., Hanaor D.A. and Gan Y. 2018. Dynamic contact angle hysteresis in liquid bridges. *Colloids and Surfaces A: Physicochemical and Engineering Aspects* **555**, 365–371.

Skempton A.W. 1954. The pore-pressure coefficients A and B. *Geotechnique* **4**, 143–147.

Spencer J.W. and Shine J. 2016. Seismic wave attenuation and modulus dispersion in sandstones. *Geophysics* **81**, D211–D231.

Tadmor R. 2004. Line energy and the relation between advancing, receding, and young contact angles. *Langmuir* **20**, 7659–7664.

Tisato N., Chapman S., Zhao Q., Grasselli G. and Quintal B. 2015. Seismic wave attenuation in rocks saturated with bubbly liquids: experiments and numerical modeling. In SEG Technical Program Expanded Abstracts (pp. 3254–3258). Society of Exploration Geophysicists.

Tisato N., Grasselli G., Quintal B. and Podladchikov Y. 2014. Seismic wave attenuation in fluid-saturated rock as result of gas dissolution. In SEG Technical Program Expanded Abstracts (pp. 1985–1990). Society of Exploration Geophysicists.

Tutuncu A.N., Podio A.L., Gregory A.R. and Sharma M.M. 1998. Nonlinear viscoelastic behavior of sedimentary rocks, Part I: Effect of frequency and strain amplitude. *Geophysics* **63**, 184–194.

Vernik L. and Kachanov M. 2012. On some controversial issues in rock physics. *The Leading Edge* **31**, 636–642.

Verwer K., Eberli G., Baechle G. and Weger R. 2010. Effect of carbonate pore structure on dynamic shear moduli. *Geophysics* **75**, E1–E8.

Waite W., Moerig R. and Spetzler H. 1997. Seismic attenuation in a partially saturated, artificial crack due to restricted contact line motion. *Geophysical Research Letters* **24**, 3309–3312.

Walsh J.B. 1965. The effect of cracks on the compressibility of rock. *Journal of Geophysical Research* **70**, 381–389.

Wang Z., Schmitt D.R. and Wang R. 2015. Does wettability influence seismic wave propagation in liquid-saturated porous rocks? *Geophysical Journal International* **203**, 2182–2188.

Wollner U. and Dvorkin J. 2018. Effective bulk modulus of the pore fluid at patchy saturation. *Geophysical Prospecting* **66**(7), 1372–1383.

Wyllie M.R.J., Gregory A.R. and Gardner G.H.F. 1958. An experimental investigation of factors affecting elastic wave velocities in porous media. *Geophysics* **23**, 459–493.

Yaminsky V.V. 2000. Molecular mechanisms of hydrophobic transitions. *Journal of Adhesion Science and Technology* **14**, 187–233.

Yarushina V.M. and Podladchikov Y.Y. 2010. Plastic yielding as a frequency and amplitude independent mechanism of seismic wave attenuation. *Geophysics* **75**, N51.

Zhang Y. 2016. *Static and dynamic behaviour of inter-granular liquid bridges: hysteresis of contact angle and capillary forces*. Master's thesis, University of Sydney.

Zhang Y., Nishizawa O., Kiyama T. and Xue Z. 2015. Saturation-path dependency of P-wave velocity and attenuation in sandstone saturated with CO_2 and brine revealed by simultaneous measurements of waveforms and X-ray computed tomography images. *Geophysics* **80**, D403–D415.

Zimmerman R.W. 1990. *Compressibility of sandstones* (Vol. **29**). Elsevier.

APPENDIX: EQUATIONS OF THE ROCK PHYSICS MODEL

In this appendix, we introduce equations describing the hysteresis of liquid bridges in an isolated partially saturated crack.

A.1 Equilibrium state

An analytical solution describing equilibrium stresses and displacements around partially saturated cracks can be found in Rozhko (2016). The half-opening of the crack aperture at a given contact line location is calculated as follows (Rozhko 2016):

$$w_a = \frac{b}{p_{\rm cl}} \left(p_{\rm cl} + \sigma + p_{\rm we} + \left(\frac{\pi - 2\beta - 2\cot(\beta)\ln[\cos(\beta)]}{\pi} \right) p_{\rm cap} \right) \sin(\beta). \tag{A1}$$

The capillary pressure is calculated using equation (A1) and the Laplace equation, $p_{\rm cap} = \frac{\gamma\cos(\theta)}{w_a}$, as follows (Rozhko 2016):

$$p_{\rm cap} = \frac{\pi}{4} \left(p_{\rm cl} + \sigma + p_{\rm we} \right) \times \frac{1 - \sqrt{1 - 8\, p_{\rm cl} \frac{\gamma\cos(\theta)}{\pi b} \frac{\left(\beta + \cot(\beta)\ln[\cos(\beta)] - \pi/2\right)}{\left(p_{\rm cl} + \sigma + p_{\rm we}\right)^2 \sin(\beta)}}}{\beta + \cot(\beta)\ln[\cos(\beta)] - \pi/2}, \tag{A2}$$

where $p_{\rm cl}$ is the crack closure pressure, calculated as (Rozhko 2016)

$$p_{\rm cl} = \frac{bE}{2a\left(1 - v^2\right)}, \tag{A3}$$

where E and v are Young's modulus and Poisson's ratio of the rock around a crack. The angle β in equations (A1) and (A2) defines the location of the contact line:

$$\cos(\beta) = \frac{c}{a}. \tag{A4}$$

The total volume of a partially saturated crack ($V_{\rm tot}$) is calculated as (Rozhko 2016)

$$\frac{V_{\rm tot}}{\pi ab} = 1 + \frac{\sigma + p_{\rm we} + \left(1 + \frac{\sin(2\beta) - 2\beta}{\pi}\right) p_{\rm cap}}{p_{\rm cl}}. \tag{A5}$$

The volume of the wetting fluid inside the partially saturated crack ($V_{\rm we}$) is calculated as (Rozhko 2016)

$$\frac{\tilde{V}_{\rm we}}{\pi ab} = \left(1 + \frac{\sigma + p_{\rm we} + p_{\rm cap}\left(1 + \frac{4}{\pi}\left[\frac{\beta\sin(2\beta) - \beta^2 + 2\cos^2(\beta)\ln[\cos(\beta)]}{2\beta - \sin(2\beta)}\right]\right)}{p_{\rm cl}} \right) \times \frac{(2\beta - \sin(2\beta))}{\pi}. \tag{A6}$$

Equations (A5) and (A6) calculate volumes per unit length in $z-$directions, perpendicular to the plane of Fig. 2; therefore, the $V_{\rm tot}$ and $\tilde{V}_{\rm we}$ in equations (A5) and (A6) have the dimension of an area.

The above equations neglect the additional small volume occupied by the non-wetting phase due to the curvature of the interface menisci. Half of this additional volume is shown in white in Fig. 4(b) for $|x| \geq c$. It is not difficult to demonstrate that this additional volume reduction can be calculated as follows:

$$\delta V_{\rm we} = -\frac{(\pi - 2\theta - \sin(2\theta))}{\cos^2(\theta)} w_a^2, \tag{A7}$$

where $\delta V_{\rm we} \ll V_{\rm we}$. Thus, corrected volumes of the wetting and non-wetting fluid phases inside the crack will be

$$V_{\rm we} = \tilde{V}_{\rm we} + \delta V_{\rm we} \tag{A8}$$

and

$$V_{\rm nw} = V_{\rm tot} - V_{\rm we}. \tag{A9}$$

The wetting phase saturation of the crack, ($S_{\rm we}$), is defined as

$$S_{\rm we} = \frac{V_{\rm we}}{V_{\rm tot}}. \tag{A10}$$

While the small correction term, $\delta V_{\rm we}$, can be neglected in the calculation of the crack saturation, it cannot be neglected in calculations of the crack stiffness (see the next section) because it affects the effective compressibility of the fluid when gas saturations are small. Saturation degree of the non-wetting phase is calculated as $S_{\rm nw} = 1 - S_{\rm we}$.

Due to the curvature of the interface menisci, the maximum value of the wetting phase saturation, predicted in the

limit when $c \to 0$ (Fig. 4a), is smaller than one. Using the above equations, it can be calculated:

$$\max\ (S_{we}) = 1 - \frac{(\pi - 2\theta - \sin(2\theta))}{\pi \cos^2(\theta)} \frac{b}{a} \left(1 + \frac{\sigma + p_{we}}{p_{cl}}\right). \tag{A11}$$

Note that $1 - \frac{b}{a} \leq \max(S_{we}) < 1$. The saturation range $\max(S_{we}) \leq S_{we} \leq 1$ is not considered by our model, because this saturation range corresponds to the transition zone between complete wetting phase saturation and entry of the non-wetting phase into the crack. A stable contact line geometry does not exist in this transition zone. Similar arguments are applied when $c \to a$ (Fig. 4a). In this case, the interface menisci cannot overlap with the crack tip. Thus, the model has the lower bound of applicability, which is similar to equation (A11) limited by $0 < \min(S_{we}) \leq \frac{b}{a}$. Hence, our model is applicable for the following saturations range of the crack:

$$\frac{b}{a} \leq S_{we} \leq 1 - \frac{b}{a}. \tag{A12}$$

In calculations, we consider very narrow cracks, $a \gg b$; thus, our model is applicable almost for the entire range of saturations.

A.2 Wave-induced perturbation of equilibrium state

Perturbation of stress and all equilibrium parameters can be split in two parts: (i) when the contact line is pinned and (ii) when the contact line is moving. Perturbation of stress is given by the equation

$$\Delta\sigma = \Delta\sigma^{(1)} + \Delta\sigma^{(2)}, \tag{A13}$$

where $\Delta\sigma^{(1)} = \Delta\sigma_c$ and $\Delta\sigma^{(2)} = \Delta\sigma - \Delta\sigma_c$.

Corresponding perturbations of equilibrium parameters are calculated as follows:

$$\Delta V_{tot} = \Delta V_{tot}^{(1)} + \Delta V_{tot}^{(2)}, \tag{A14}$$

$$\Delta V_{we} = \Delta V_{we}^{(1)} + \Delta V_{we}^{(2)}, \tag{A15}$$

$$\Delta p_{we} = \Delta p_{we}^{(1)} + \Delta p_{we}^{(2)}, \tag{A16}$$

$$\Delta p_{cap} = \Delta p_{cap}^{(1)} + \Delta p_{cap}^{(2)}, \tag{A17}$$

$$\Delta c = \Delta c^{(1)} + \Delta c^{(2)} \tag{A18}$$

and

$$\Delta\theta = \Delta\theta^{(1)} + \Delta\theta^{(2)}. \tag{A19}$$

Note here that $\Delta c^{(1)} = 0$ and $\Delta\theta^{(2)} = 0$; therefore, $\Delta c = \Delta c^{(2)}$ and $\Delta\theta = \Delta\theta^{(1)}$. When $\Delta\sigma$ is applied, first, the interface meniscus deforms to its extreme value (θ_a or θ_r, depending on the polarity of stress perturbation and compressibilities of immiscible fluid phases) and second, the contact line will move without changing the contact angle. The bending and moving directions of the interface meniscus and contact line must coincide. The initial contact angle is assumed to be equal to the equilibrium Young's angle, that is, $\theta_0 = \theta_Y$. In the first part, when a critical stress perturbation $\Delta\sigma^{(1)} = \Delta\sigma_c$ is applied, the contact angle will change from the initial angle θ_0 to its maximum or minimum value. The maximum or minimum value for the contact angle corresponds to the advancing or receding contact angle (θ_a or θ_r). In the second part, with further increase of stress perturbation, the contact line will slip with the advancing or receding angle. We consider a low frequency limit when a slip velocity is quasi-static, that is, when θ_a and θ_r are constant values.

In the next two subsections, we define the complete set of equations, which will allow us to find the wave-induced perturbations of the following parameters: ΔV_{tot}, ΔV_{we}, Δp_{we}, Δp_{cap}, Δc, $\Delta\theta$.

A.2.1 Part 1: Bending of the interface meniscus

In this section, we will present equations for the case when the contact line is pinned to the crack surface and wave-induced deformations cause bending of the liquid–gas interface meniscus due to the change of the contact angle and deformation of the crack aperture. Using a linear elasticity assumption, we will find the following perturbations: $\Delta V_{tot}^{(1)}$, $\Delta V_{we}^{(1)}$, $\Delta p_{we}^{(1)}$, $\Delta p_{cap}^{(1)}$ and $\Delta\theta$ caused by an applied stress perturbation $\Delta\sigma^{(1)}$. Here, we consider that the contact line is fixed, that is, $\Delta c^{(1)} = 0$, which also implies $\Delta\beta = 0$, according to equation (A4).

Equations (2) and (3) can be rewritten in the form (using equations (1) and (A9)):

$$\Delta V_{we}^{(1)} K_{we} = -V_{we}\, \Delta p_{we}^{(1)}, \tag{A20}$$

and

$$\left(\Delta V_{tot}^{(1)} - \Delta V_{we}^{(1)}\right) K_{nw} = -(V_{tot} - V_{we})\left(\Delta p_{we}^{(1)} + \Delta p_{cap}^{(1)}\right). \tag{A21}$$

Next, let us consider Taylor's expansions for capillary pressure, p_{cap}; total volume of partially saturated crack, V_{tot};

and volume of the wetting phase inside a partially saturated crack, V_{we}:

$$\Delta p_{cap}^{(1)} = \frac{\partial p_{cap}}{\partial \sigma}\ \Delta\sigma^{(1)} + \frac{\partial p_{cap}}{\partial p_{we}}\Delta p_{we}^{(1)} + \frac{\partial p_{cap}}{\partial \theta}\ \Delta\theta, \tag{A22}$$

$$\Delta V_{tot}^{(1)} = \frac{\partial V_{tot}}{\partial \sigma}\ \Delta\sigma^{(1)} + \frac{\partial V_{tot}}{\partial p_{we}}\Delta p_{we}^{(1)} + \frac{\partial V_{tot}}{\partial p_{cap}}\Delta p_{cap}^{(1)} \tag{A23}$$

and

$$\Delta V_{we}^{(1)} = \frac{\partial V_{we}}{\partial \sigma}\ \Delta\sigma^{(1)} + \frac{\partial V_{we}}{\partial p_{we}}\Delta p_{we}^{(1)} + \frac{\partial V_{we}}{\partial p_{cap}}\Delta p_{cap}^{(1)} + \frac{\partial V_{we}}{\partial \theta}\ \Delta\theta. \tag{A24}$$

All partial derivatives are calculated analytically in Appendix A.3, using analytical solutions for p_{cap}, V_{tot} and V_{we}, presented in Section A.1. Equations (A20)–(A24) are five linear equations, which have a unique solution for the following five unknown parameters: $\Delta V_{tot}^{(1)}$, $\Delta V_{we}^{(1)}$, $\Delta p_{we}^{(1)}$, $\Delta p_{cap}^{(1)}$ and $\Delta\theta$. With the application of a stress perturbation $\Delta\sigma^{(1)}$, the contact angle will be changed as follows: $\theta = \theta_0 + \Delta\theta$, where $\Delta\theta$ could be positive or negative, depending on $\Delta\sigma^{(1)}$ and the fluid properties. The range of possible values for the contact angle is limited by the advancing and receding angles: $\theta_r \le \theta \le \theta_a$. It will not be possible to bend the interface meniscus further when the contact angle has reached $\theta = \theta_a$ or $\theta = \theta_r$. At this point, the contact line will start to slip. Substituting $\Delta\sigma^{(1)} = \Delta\sigma_c$ and $\Delta\theta = \theta_a - \theta_0$ (or $\Delta\theta = \theta_r - \theta_0$) in equations (A20)–(A24) allows us to find the critical stress perturbation $\Delta\sigma_c$. Analytical solutions for $\Delta\sigma_c$ and other parameters can be written in the matrix form as follows:

$$\begin{pmatrix} \Delta\sigma_c \\ \Delta p_{cap}^{(1)} \\ \Delta p_{we}^{(1)} \\ \Delta V_{tot}^{(1)} \\ \Delta V_{we}^{(1)} \end{pmatrix} = -\ \Delta\theta \begin{pmatrix} 0 & 0 & V_{we} & 0 & K_{we} \\ 0 & V_{tot}-V_{we} & V_{tot}-V_{we} & K_{nw} & -K_{nw} \\ \partial p_{cap}/\partial\sigma & -1 & \partial p_{cap}/\partial p_{we} & 0 & 0 \\ \partial V_{tot}/\partial\sigma & \partial V_{tot}/\partial p_{cap} & \partial V_{tot}/\partial p_{we} & -1 & 0 \\ \partial V_{we}/\partial\sigma & \partial V_{we}/\partial p_{cap} & \partial V_{we}/\partial p_{we} & 0 & -1 \end{pmatrix}^{-1} \times \begin{pmatrix} 0 \\ 0 \\ \partial p_{cap}/\partial\theta \\ 0 \\ \partial V_{we}/\partial\theta \end{pmatrix}. \tag{A25}$$

If $|\Delta\sigma| > |\Delta\sigma_c|$, the contact line will move and we need to use additional equations from the next section. If $|\Delta\sigma| \le |\Delta\sigma_c|$, the contact line will not move, but the interface meniscus will deform. The general solution of equations (A20)–(A24) is given in the following form:

$$\begin{pmatrix} \Delta\theta \\ \Delta p_{cap}^{(1)} \\ \Delta p_{we}^{(1)} \\ \Delta V_{tot}^{(1)} \\ \Delta V_{we}^{(1)} \end{pmatrix} = -\ \Delta\sigma^{(1)} \begin{pmatrix} 0 & 0 & V_{we} & 0 & K_{we} \\ 0 & V_{tot}-V_{we} & V_{tot}-V_{we} & K_{nw} & -K_{nw} \\ \partial p_{cap}/\partial\theta & -1 & \partial p_{cap}/\partial p_{we} & 0 & 0 \\ 0 & \partial V_{tot}/\partial p_{cap} & \partial V_{tot}/\partial p_{we} & -1 & 0 \\ \partial V_{we}/\partial\theta & \partial V_{we}/\partial p_{cap} & \partial V_{we}/\partial p_{we} & 0 & -1 \end{pmatrix}^{-1} \times \begin{pmatrix} 0 \\ 0 \\ \partial p_{cap}/\partial\sigma \\ \partial V_{tot}/\partial\sigma \\ \partial V_{we}/\partial\sigma \end{pmatrix}. \tag{A26}$$

The solution of this system of equations is dependent on four independent variables: the contact angle θ, the applied far-field stress σ, the pressure in the wetting (water) phase p_{we}, and the position of the contact line β. All matrix coefficients of equations (A25) and (A26) are calculated for the following independent variables: $\theta = \theta_0, \sigma = \sigma_0, p_{we} = p_{we\,0}$ and $\beta = \beta_0$. After calculations of this part, the independent variables will be changed to $\theta = \theta + \Delta\theta$, $\sigma = \sigma + \Delta\sigma^{(1)}$, $p_{we} = p_{we} + \Delta p_{we}^{(1)}$ and $\beta = \beta + 0$.

A.2.2 Part 2: Contact line motion

In this section, we present equations for the case when the contact line is mobilized, assuming that the contact angle θ is equal to either θ_a or θ_r and does not change during contact line motion ($\Delta\theta^{(2)} = 0$). Next, we will calculate the following perturbations: $\Delta V_{tot}^{(2)}$, $\Delta V_{we}^{(2)}$, $\Delta p_{we}^{(2)}$, $\Delta p_{cap}^{(2)}$, $\Delta c^{(2)} = \Delta c$ and $\Delta\beta^{(2)} = \Delta\beta$, caused by an applied stress perturbation $\Delta\sigma^{(2)}$.

Considering a Taylor's expansion of equation (A4), we can write

$$\Delta c = -a\sin(\beta)\,\Delta\beta. \tag{A27}$$

Similar to equations (A20) and (A21), we can write

$$\Delta V_{we}^{(2)} K_{we} = -V_{we}\,\Delta p_{we}^{(2)} \tag{A28}$$

and

$$\left(\Delta V_{tot}^{(2)} - \Delta V_{we}^{(2)}\right) K_{nw} = -\left(V_{tot} - V_{we}\right)\left(\Delta p_{we}^{(2)} + \Delta p_{cap}^{(2)}\right). \tag{A29}$$

Taylor's expansions of p_{cap}, V_{tot} and V_{we} are different from part 1, because in part 2, $\Delta c \neq 0$ and $\Delta\theta = 0$, while in part 1, $\Delta c = 0$ and $\Delta\theta \neq 0$. The expressions for Taylor's expansions are written as follows:

$$\Delta p_{cap}^{(2)} = \frac{\partial p_{cap}}{\partial \sigma}\ \Delta\sigma^{(2)} + \frac{\partial p_{cap}}{\partial p_{we}}\Delta p_{we}^{(2)} + \frac{\partial p_{cap}}{\partial \beta}\ \Delta\beta, \tag{A30}$$

$$\Delta V_{\text{tot}}^{(2)} = \frac{\partial V_{\text{tot}}}{\partial \sigma}\,\Delta\sigma^{(2)} + \frac{\partial V_{\text{tot}}}{\partial p_{\text{we}}}\Delta p_{we}^{(2)} + \frac{\partial V_{\text{tot}}}{\partial \beta}\,\Delta\beta + \frac{\partial V_{\text{tot}}}{\partial p_{\text{cap}}}\Delta p_{\text{cap}}^{(2)} \tag{A31}$$

and

$$\Delta V_{\text{we}}^{(2)} = \frac{\partial V_{\text{we}}}{\partial \sigma}\,\Delta\sigma^{(2)} + \frac{\partial V_{\text{we}}}{\partial p_{\text{we}}}\Delta p_{\text{we}}^{(2)} + \frac{\partial V_{\text{we}}}{\partial \beta}\Delta\beta + \frac{\partial V_{\text{we}}}{\partial p_{\text{cap}}}\Delta p_{\text{cap}}^{(2)}. \tag{A32}$$

All partial derivatives are calculated analytically in A.3.

$$\begin{pmatrix} \Delta\beta \\ \Delta p_{\text{cap}}^{(2)} \\ \Delta p_{\text{we}}^{(2)} \\ \Delta V_{\text{tot}}^{(2)} \\ \Delta V_{\text{we}}^{(2)} \end{pmatrix} = -\,\Delta\sigma^{(2)} \begin{pmatrix} 0 & 0 & V_{\text{we}} & 0 & K_{\text{we}} \\ 0 & V_{\text{tot}} - V_{\text{we}} & V_{\text{tot}} - V_{\text{we}} & K_{\text{nw}} & -K_{\text{nw}} \\ \partial p_{\text{cap}}/\partial\beta & -1 & \partial p_{\text{cap}}/\partial p_{\text{we}} & 0 & 0 \\ \partial V_{\text{tot}}/\partial\beta & \partial V_{\text{tot}}/\partial p_{\text{cap}} & \partial V_{\text{tot}}/\partial p_{\text{we}} & -1 & 0 \\ \partial V_{\text{we}}/\partial\beta & \partial V_{\text{we}}/\partial p_{\text{cap}} & \partial V_{\text{we}}/\partial p_{\text{we}} & 0 & -1 \end{pmatrix}^{-1} \times \begin{pmatrix} 0 \\ 0 \\ \partial p_{\text{cap}}/\partial\sigma \\ \partial V_{\text{tot}}/\partial\sigma \\ \partial V_{\text{we}}/\partial\sigma \end{pmatrix}. \tag{A33}$$

Here again, all matrix coefficients of equation (A33) are calculated at the point of independent variables: θ, σ, p_{we} and β, which were updated in calculations of part 1. After part 2, these independent variables will be updated in the following way: $\theta = \theta + 0$, $\sigma = \sigma + \Delta\sigma^{(2)}$, $p_{we} = p_{we} + \Delta p_{\text{we}}^{(2)}$ and $\beta = \beta + \Delta\beta$. Here, we presented a bilinear approximation to model the deformation of the interface meniscus and contact line motion caused by a change of stress ($\Delta\sigma$). Note that we do not prescribe the polarity (sign) of the stress perturbation during loading phase; it can be either positive or negative. During unloading, we consider a stress perturbation with opposite sign ($-\Delta\sigma$), as well as a change in initial values of independent variables caused by the preceding loading sequence.

A.3 Partial derivatives

In this section, we derive partial derivatives of p_{cap}, V_{tot} and $V_{\text{we}} = \tilde{V}_{\text{we}} + \delta V_{\text{we}}$, which are used in equations of sections A.2.1 and A.2.2.

First, we will start with partial derivatives of p_{cap}. To simplify equations, we introduce the following auxiliary parameters X and Y:

$$X = 1 - 8\,p_{\text{cl}}\frac{\gamma\cos(\theta)}{\pi b}\frac{\left(\beta + \cot(\beta)\ln[\cos(\beta)] - \frac{\pi}{2}\right)}{(p_{\text{cl}} + \sigma + p_{\text{we}})^2\sin(\beta)} \tag{A34}$$

and

$$Y = \beta + \cot(\beta)\ln[\cos(\beta)] - \frac{\pi}{2}. \tag{A35}$$

Partial derivatives of capillary pressure are calculated as follows:

$$\frac{\partial p_{\text{cap}}}{\partial\beta} = \frac{\pi\,(p_{\text{cl}} + \sigma + p_{\text{we}})}{8\sin(\beta)\,Y\sqrt{X}} \times \left((X-1)\cos(\beta) - \frac{\left(\sqrt{X}-1\right)^2\ln[\cos(\beta)]}{\sin(\beta)\,Y}\right), \tag{A36}$$

$$\frac{\partial p_{\text{cap}}}{\partial\sigma} = \frac{\pi}{4Y}\left(1 - \sqrt{X} - \frac{1-X}{\sqrt{X}}\right), \tag{A37}$$

$$\frac{\partial p_{\text{cap}}}{\partial p_{\text{we}}} = \frac{\partial p_{\text{cap}}}{\partial\sigma} \tag{A38}$$

and

$$\frac{\partial p_{\text{cap}}}{\partial\theta} = \frac{\pi\,(X-1)\,(p_{\text{cl}} + \sigma + p_{\text{we}})}{8Y\sqrt{X}}\,\tan(\theta). \tag{A39}$$

Next, we calculate partial derivatives of V_{tot}.

$$\frac{\partial V_{\text{tot}}}{\partial\beta} = \frac{2ab}{p_{\text{cl}}}\,(\cos(2\beta) - 1)\,p_{\text{cap}}, \tag{A40}$$

$$\frac{\partial V_{\text{tot}}}{\partial p_{\text{cap}}} = \frac{\pi ab}{p_{\text{cl}}}\left(1 + \frac{\sin(2\beta) - 2\beta}{\pi}\right), \tag{A41}$$

$$\frac{\partial V_{\text{tot}}}{\partial\sigma} = \frac{\pi ab}{p_{\text{cl}}}, \tag{A42}$$

$$\frac{\partial V_{\text{tot}}}{\partial p_{\text{we}}} = \frac{\partial V_{\text{tot}}}{\partial\sigma} \tag{A43}$$

and

$$\frac{\partial V_{\text{tot}}}{\partial\theta} = 0. \tag{A44}$$

And, finally, we calculate partial derivatives for $V_{\text{we}} = \tilde{V}_{\text{we}} + \delta V_{\text{we}}$. We start with $\tilde{V}_{\text{we}}$:

$$\frac{\partial \tilde{V}_{\text{we}}}{\partial\beta} = \frac{2ab}{p_{\text{cl}}}\left(p_{\text{cl}} + \sigma + p_{\text{we}} + \frac{p_{\text{cap}}}{\pi}\left(\pi - 4\beta - \frac{4\sin(2\beta)\ln[\cos(\beta)]}{(1-\cos(2\beta))}\right)\right) \times (1 - \cos(2\beta)), \tag{A45}$$

$$\frac{\partial \tilde{V}_{we}}{\partial p_{cap}} = \frac{ab}{p_{cl}} \times \left(1 + \frac{4}{\pi}\left[\frac{\beta \sin(2\beta) - \beta^2 + 2\cos^2(\beta)\ln[\cos(\beta)]}{2\beta - \sin(2\beta)}\right]\right) \times (2\beta - \sin(2\beta)), \quad \text{(A46)}$$

$$\frac{\partial \tilde{V}_{we}}{\partial \sigma} = \frac{ab}{p_{cl}}\ (2\beta - \sin(2\beta)), \quad \text{(A47)}$$

$$\frac{\partial \tilde{V}_{we}}{\partial p_{we}} = \frac{\partial \tilde{V}_{we}}{\partial \sigma} \quad \text{(A48)}$$

and

$$\frac{\partial \tilde{V}_{we}}{\partial \theta} = 0. \quad \text{(A49)}$$

And continue with δV_{we}:

$$\frac{\partial \delta V_{we}}{\partial p_{cap}} = \left(\pi - 2\beta - 2\cot(\beta)\ \ln[\cos(\beta)]\right)\ \frac{b\sin(\beta)}{\pi\, p_{cl}}\ \frac{2\delta V_{we}}{w_a}, \quad \text{(A50)}$$

$$\frac{\partial \delta V_{we}}{\partial \sigma} = 2b\sin(\beta)\ \frac{\delta V_{we}}{p_{cl} w_a}, \quad \text{(A51)}$$

$$\frac{\partial \delta V_{we}}{\partial p_{we}} = \frac{\partial \delta V_{we}}{\partial \sigma}\ , \quad \text{(A52)}$$

$$\frac{\partial \delta V_{we}}{\partial \theta} = -w_a^2 \frac{((\pi - 2\theta)\ \tan(\theta) - 2)}{\cos^2(\theta)} \quad \text{(A53)}$$

and

$$\frac{\partial \delta V_{we}}{\partial \beta} = \frac{2\delta V_{we}}{w_a\ p_{cl}}\ b\cos(\beta)\left(p_{cl} + \sigma + p_{we} + \frac{p_{cap}}{\pi}\left(\pi - 2\beta + 2\tan(\beta)\ln[\cos(\beta)]\right)\right). \quad \text{(A54)}$$

A.4 Applicability of the model for large contact angle hysteresis

In this section, we will discuss the applicability of the proposed model. Taylor's expansions and partial derivatives, calculated in the previous sections, imply that changes of all parameters are small, including the change in contact angle. However, experimental data, reported by Ethington (1990), suggest that a contact angle hysteresis of water–air interface on calcite, quartz, and biotite surfaces could be as much as 40°, that is, $\theta_a - \theta_r \sim 40^\circ = 0.3491$ radians. Thus, the value of $\Delta\theta = \theta_a - \theta_0 \sim 20^\circ$ may be outside the validity envelope of the system of linearized equations, derived from Section A.2.1. In order to get more accurate results, the contact angle perturbation $\Delta\theta = \theta_a - \theta_0$ can be subdivided in N smaller intervals, $\widetilde{\Delta\theta} = \frac{\theta_a - \theta_0}{N}$, and the set of linearized equations of Section A.2.1 is solved subsequently for N perturbation steps $\widetilde{\Delta\theta} \ll 1$. A similar approach is used if the perturbation of the contact line location, $\Delta\beta$, is getting large. In this case, the stress perturbation $\Delta\sigma^{(2)}$ can be subdivided in N smaller intervals, $\widetilde{\Delta\sigma^{(2)}} = \frac{\Delta\sigma^{(2)}}{N}$, and the set of linearized equations of Section A.2.2 is solved subsequently for N perturbation steps $\widetilde{\Delta\sigma^{(2)}}$. Calculations following this approach are implemented in the Matlab.

A.5 Single-phase compressibility

In this section, we derive equation (14), considering that the crack is fully saturated by a single-phase fluid with effective properties. In this case, the capillary pressure in equation (A5) is neglected, and the total crack volume (V_{tot}) is calculated as follows:

$$\frac{V_{tot}}{\pi ab} = 1 + \frac{\sigma + p_{fl}}{p_{cl}}. \quad \text{(A55)}$$

Equations (A20) and (A21), representing undrained boundary conditions for two-phase fluids inside the crack, are reduced to the following equation:

$$\Delta V_{tot}\ K_{fl} = -V_{tot}\,\Delta p_{fl}. \quad \text{(A56)}$$

While the perturbation of the crack volume is calculated using equation, similar to equation (A23), in which the capillary pressure is neglected:

$$\Delta V_{tot} = \frac{\partial V_{tot}}{\partial \sigma}\ \Delta\sigma + \frac{\partial V_{tot}}{\partial p_{fl}}\Delta p_{fl}. \quad \text{(A57)}$$

Next, using equations (A56) and (A57), we get

$$\frac{\Delta V_{tot}}{\Delta\sigma} = \frac{\frac{\partial V_{tot}}{\partial \sigma}}{\left(1 + \frac{K_{fl}}{V_{tot}}\frac{\partial V_{tot}}{\partial p_{fl}}\right)}. \quad \text{(A58)}$$

Next, by combining equations (A58), (4), (5), (6), (A42) and (A43), we derive equation (14).

A.6 Different boundary conditions on immiscible fluids

In this paper, we developed a rock physics model for isolated partially saturated crack and discussed in the introduction that the depinning of the contact line strongly depends on many parameters, given in Table 1, including wave amplitude and the pore-fluid system. We also discussed in the introduction

that much greater wave amplitudes are required for the contact line slippage in the crack, partially saturated with an oil and water system. Using the theoretical model, developed in this paper, it is possible to demonstrated that the contact line will slip in a crack, partially saturated with oil and water if different boundary conditions on fluids are used. If the crack is not isolated, but connected with matrix pores, the seismic wave will induce two-phase fluid flow between the crack and the matrix (Pride *et al.* 2004; Müller *et al.* 2011). In this case, when both matrix and crack pores are connected, it is relevant to consider drained versus undrained boundary conditions in the model (Mavko *et al.* 2009). During drained (unjacketed) boundary conditions, pore fluids can flow freely in or out of the sample (or representative elementary volume) to ensure constant pore pressure in each fluid phase, that is,

$$\Delta p_{\mathrm{we}} = 0 \tag{A59}$$

and

$$\Delta p_{\mathrm{nw}} = 0. \tag{A60}$$

During undrained (jacketed) boundary conditions, the fluids cannot flow in or flow out of the sample (or representative elementary volume). In this case, wave-induced changes of fluid pressure are described by two Skempton's coefficients B_{we} and B_{nw} for the wetting and non-wetting phases as follows (Skempton 1954; Pride *et al.* 2004; Müller *et al.* 2011; Fredlund, Rahardjo and Fredlund 2012):

$$\Delta p_{\mathrm{we}} = -B_{\mathrm{we}}\Delta\sigma \tag{A61}$$

and

$$\Delta p_{\mathrm{nw}} = -B_{\mathrm{nw}}\Delta\sigma, \tag{A62}$$

where $0 \leq B_{\mathrm{we}} \leq 1$ and $0 \leq B_{\mathrm{nw}} \leq 1$. Note here that we use a sign convention when compressive stresses and compressive strains are negative, while fluid pressure is positive. In the partially saturated rock, the coefficients B_{we} and B_{nw} are not the material constants, but coefficients that may depend on the saturation (Fredlund *et al.* 2012). Thus, these parameters can be used phenomenologically.

Using equations (A59)–(A60) or (A61)–(A62) instead of equations (2)–(3), it is possible to demonstrate that in the water–oil system the critical stress ($\Delta\sigma_c$), required for slippage of the contact line, is in the range 10^2 to 10^4 Pa, that is, typical for linear seismic waves.